

**UC Berkeley**  
**SEMM Reports Series**

**Title**

An Assessment of the Cap Model: Consistent Return Algorithms and Rate-Dependent Extension

**Permalink**

<https://escholarship.org/uc/item/0jb9x5sn>

**Authors**

Simo, Juan

Ju, Jiann-Wen

Pister, Karl

et al.

**Publication Date**

1985-05-01

#14  
REPORT

REPORT NO.  
UCB/SESM-85/5

STRUCTURAL ENGINEERING AND  
STRUCTURAL MECHANICS

AN ASSESSMENT OF THE  
CAP MODEL: CONSISTENT  
RETURN ALGORITHMS AND  
RATE-DEPENDENT  
EXTENSION

by

JUAN C. SIMO

JIANN-WEN JU

KARL S. PISTER

ROBERT L. TAYLOR

MAY 1985

DEPARTMENT OF CIVIL ENGINEERING  
UNIVERSITY OF CALIFORNIA  
BERKELEY, CALIFORNIA

# *An Assessment of the Cap Model: Consistent Return Algorithms and Rate-Dependent Extension*

JUAN C. SIMO JIANN-WEN JU  
KARL S. PISTER ROBERT L. TAYLOR

Department of Civil Engineering  
University of California, Berkeley

## Abstract

In this paper, the *inviscid* two-invariant cap model and a viscoplastic *rate-dependent* generalization are considered. The algorithmic implementation of the model is first considered in detail. For the *inviscid* case, a new algorithm is proposed based on the notion of closest point projection. *Exact* satisfaction of the consistency condition is shown to reduce to a single scalar equation that may be solved by iterative methods. Special attention is given to the singular corner region at the intersection of cap and failure surfaces. For this situation, it is shown that existing procedures may lead to errors of more than 50%, even for moderate strain increments. Iso-error maps for the "Colorado concrete" data are developed to demonstrate the good accuracy of the proposed closest point projection procedure, even for large strain increments compared with characteristic strains at yielding.

A viscoplastic extension of the cap model of the Perzyna type is also presented, and the appropriate extension of the closest point algorithm developed for the *inviscid* case is considered. This algorithm is considerably simpler than viscoplastic algorithms initially proposed by Hughes and Taylor and subsequently employed by Katona for the cap model.

The predictive capabilities of the cap model are assessed through extensive simulation based on well-documented "Colorado" experimental data. To systematically fit the model to experimental data, an optimization procedure based on the Marquardt-Levenberg algorithm is developed.

## Contents

1. Introduction
  2. Original (*inviscid*) cap model algorithm
    - 2.1. Basic formulation
    - 2.2. Analysis of the existing algorithm
    - 2.3. Treatment of the singular corner region
  3. Closest point projection algorithm. *Inviscid* case
    - 3.1. Formulation of the algorithm
    - 3.2. Consistent treatment of the singular corner region
    - 3.3. Accuracy analysis. Iso-error maps
  4. Viscoplastic (*rate-dependent*) extension
    - 4.1. Basic formulation and algorithm
  5. Parameter estimation and numerical simulations
    - 5.1. Parameter estimation. Marquardt-Levenberg algorithm
    - 5.2. *Inviscid* case. "Colorado" concrete data
    - 5.3. Some rate-dependent simulations
  6. Closure
- References

# *An Assessment of the Cap Model: Consistent Return Algorithms and Rate-Dependent Extension*

JUAN C. SIMO JIANN-WEN JU  
KARL S. PISTER ROBERT L. TAYLOR

Department of Civil Engineering  
University of California, Berkeley

## 1. Introduction

Current numerical simulations employing the inviscid, two-invariant associative cap model originally proposed by DiMaggio and Sandler [1,2] are based on the algorithm developed by Sandler and Rubin [3]. This algorithm allows for considerable flexibility in the choice of functional forms for the yield condition and hardening law with minor coding changes. Thus, it is applied to a wide range of geomaterials.

It has been shown [4-6] that the notion of operator split can be efficiently used to develop algorithms which are a) consistent with the "continuum" elastoplastic constitutive equations and b) unconditionally stable with respect to step sizes. These algorithms are often referred to as closest point projections or return mapping algorithms, and include, as a particular case, the well-known radial return method of Wilkins [7]. It is shown below that the algorithm proposed by Sandler and Rubin, although within the class of return mapping procedures, is not fully consistent with the notion of closest point projection, thus violating the normality condition of the plastic flow rule. It is further shown that the integration procedure advocated by these authors in the *singular corner region* lying in the vicinity of the intersection of the failure envelope and cap, prevents plastic dilatancy and may lead to errors of more than 50%. These shortcomings motivate the present proposal of a "revised" cap algorithm which is fully consistent with the notion of closest point return mapping, thus preserving normality of the plastic flow, and furnishing the correct procedure in the singular corner region. The accuracy of the proposed procedure is assessed by means of iso-error maps which illustrate the good accuracy of the algorithm even for large strain increments compared with characteristic strains at yielding. Comparisons between the "original" and the "revised" cap model algorithms are also given.

The original *inviscid* cap model is extended to account for rate effects by means of a viscoplastic regularization of the type proposed by Perzyna [8]. Viscoplastic extensions of this type have a long history in the computational literature (see e.g. Zienkiewicz and Cormeau [9], Hughes and Taylor [10], Pinsky, Ortiz and Pister [11], Simo, Hjelmstad and Taylor [12]). For the cap model, a viscoplastic extension of this type has recently been considered by Katona [13]. The algorithmic treatment advocated by Katona relies heavily on the implicit

procedure developed by Hughes and Taylor [10], which involves the solution of a nonlinear system of equations for each iteration within a given time step. The procedure developed here, on the other hand, is based on the notion of operator split and closest point projection, as proposed in Simo and Ortiz [5], and results in the solution of a single nonlinear scalar equation. Preliminary numerical simulations of the viscoplastic cap model developed in this paper are also given.

To assess the predictive capabilities of the inviscid cap model, the extensive and well-documented data obtained in the experimental program at the University of Colorado [16] has been selected. A characteristic of this experimental work is the exercise of truly three dimensional non-conventional stress paths. Due to the non-conventional nature of the experimental data, standard fitting procedures based on the use of conventional tests to independently fit cap, failure envelope and hardening law (see e.g. [17,18]) cannot be used. Hence, to obtain an optimal fit for the cap parameters an alternative constrained optimization procedure which employs a modified Marquardt-Levenberg algorithm is developed. This approach makes the fitting process completely systematic and renders the optimal values of the parameters in a least square sense.

In the simulations reported herein, six (6) tests are used to fit the seven parameters of the cap model, and the resulting model is exercised to predict the remaining sixty-one (61) tests. The resulting predictions agree remarkably well with the experimental results.

## 2. Original (inviscid) cap model algorithm

In this section, we first summarize the basic constitutive equations governing the two-invariant rate-independent model as originally proposed by DiMaggio and Sandler [1]. Subsequently, we discuss the algorithmic treatment of this model advocated by Sandler and Rubin [3].

### 2.1 Basic formulation

The two-invariant, rate-independent elastoplastic associative cap model is characterized by the following constitutive equations:

$$\begin{aligned}
 \boldsymbol{\epsilon} &= \boldsymbol{\epsilon}^e + \boldsymbol{\epsilon}^p \\
 \boldsymbol{\sigma} &= \hat{\boldsymbol{\sigma}}(\boldsymbol{\epsilon}^e) \quad (\text{elastic response}) \\
 \dot{\boldsymbol{\epsilon}}^p &= \dot{\lambda} \frac{\partial \phi(\boldsymbol{\sigma}, \kappa)}{\partial \boldsymbol{\sigma}} \quad (\text{associative flow rule}) \\
 \phi(\boldsymbol{\sigma}, \kappa) &\leq 0 \quad (\text{yield condition})
 \end{aligned} \tag{2.1}$$

where  $\boldsymbol{\epsilon}$ ,  $\boldsymbol{\epsilon}^e$ , and  $\boldsymbol{\epsilon}^p$  denote the total, elastic and plastic strain tensors;  $\boldsymbol{\sigma}$  denotes the stress tensor and  $\phi(\boldsymbol{\sigma}, \kappa) = 0$  is the yield surface in stress space. In addition,  $\kappa$  is the hardening parameter which for the cap model is related to the plastic volume change by a *hardening law* as

described below. Loading/unloading conditions may be expressed in a compact manner by requiring that

$$\phi(\boldsymbol{\sigma}, \kappa) \leq 0, \quad \dot{\lambda} \geq 0, \quad \dot{\lambda} \phi(\boldsymbol{\sigma}, \kappa) \equiv 0 \quad (2.2)$$

This is the so-called Kuhn-Tucker form of unilateral constraint conditions. Note that if  $\phi < 0$  then  $\dot{\lambda} = 0$  and the process is elastic. On the other hand, for loading,  $\dot{\lambda} > 0$  and  $\phi = 0$ . In this latter case,  $\lambda$  is determined by requiring that  $\dot{\phi} = 0$ ; the so-called *consistency condition* leads to the classical elastoplastic tangent moduli.

The basic characteristic of the cap model is the form of the yield function  $\phi(\boldsymbol{\sigma}, \kappa)$  which is specified in terms of two functions  $F_e$  and  $F_c$ . The function  $F_e$  denotes the so-called *failure envelope surface* whereas the function  $F_c$  is referred to as the *hardening cap*. Functional forms for  $F_e$  and  $F_c$  are (see Fig. 1)

$$\phi(\boldsymbol{\sigma}, \kappa) \equiv \begin{cases} \sqrt{J_{2D}} - F_e(J_1) \leq 0 & \text{(failure envelope)} \\ \sqrt{J_{2D}} - F_c(J_1, \kappa) \leq 0 & \text{(cap surface)} \end{cases} \quad (2.3)$$

where  $J_1 \equiv \text{tr } \boldsymbol{\sigma}$ ,  $J_{2D} \equiv \frac{1}{2} \mathbf{s} : \mathbf{s}$  ( $\mathbf{s}$  : stress deviator) and

$$F_e(J_1) \equiv \alpha - \gamma \exp(-\beta J_1) + \Theta J_1$$

$$F_c(J_1, \kappa) \equiv \frac{1}{R} \sqrt{[X(\kappa) - L(\kappa)]^2 - [J_1 - L(\kappa)]^2} \quad (2.4)$$

$$L(\kappa) \equiv \langle \kappa \rangle = \begin{cases} \kappa & \text{if } \kappa > 0 \\ 0 & \text{if } \kappa \leq 0 \end{cases} \quad (\text{McAuley bracket})$$

Finally, the *hardening parameter*  $\kappa$  is related to the *plastic volume change*  $\epsilon_v^p \equiv \text{tr } \boldsymbol{\epsilon}^p$  by the hardening law

$$\epsilon_v^p(X) \equiv W \{ 1 - \exp[-D X(\kappa)] \} \quad (2.5)$$

where  $X(\kappa)$  is defined by

$$X(\kappa) \equiv \kappa + R F_e(\kappa) \quad (2.6)$$

In the above expressions,  $\alpha, \beta, \gamma, \Theta, W, D$ , and  $R$  are material parameters which characterize the two-invariant cap model considered here.

In the original version of the cap model algorithm, four basic response modes are considered: (a) *elastic mode*, (b) *tension cutoff mode*, (c) *failure envelope mode*, and (d) *cap mode*. The inconsistency in the algorithm proposed in [3] arises in the failure envelope mode where consistency is only enforced in a *linearized sense* and normality of the plastic flow is violated.

## 2.2 Analysis of the existing algorithm

It is shown below that the derivation for the failure envelope mode given in [3] is only the first step of an iterative return mapping algorithm proposed in [5] and further analyzed in [6]. To see this, it suffices to determine the evolution of the governing quantity,  $\Delta\epsilon_v^p \equiv \text{tr} \Delta[\epsilon_{n+1}^p - \epsilon_n^p]$ , as follows. The associative flow rule (2.1)<sub>3</sub> is integrated over a typical time step  $[t_n, t_{n+1}]$  by an implicit (backward difference) scheme leading to

$$\Delta\epsilon_{n+1}^p = \Delta t \dot{\epsilon}_{n+1}^p = \lambda \Delta t \left. \frac{\partial \phi}{\partial \boldsymbol{\sigma}} \right|_{n+1} = \Delta \lambda \left[ \frac{\boldsymbol{s}}{2\sqrt{J_{2D}}} - \frac{dF_e}{dJ_1} \mathbf{1} \right] \Big|_{n+1} \quad (2.7)$$

where use has been made of (2.3). The deviatoric and volumetric parts of the plastic strain tensor at  $t_{n+1}$  are thus given by

$$\begin{aligned} \Delta \mathbf{e}_{n+1}^p &= \Delta \lambda \frac{\boldsymbol{s}}{2\sqrt{J_{2D}}} \Big|_{n+1} \\ \Delta \epsilon_v^p \Big|_{n+1} &= -3\Delta \lambda_{n+1} \frac{dF_e}{dJ_1} \Big|_{J_{1,n+1}} \end{aligned} \quad (2.8)$$

Here,  $\mathbf{e} \equiv \boldsymbol{\epsilon} - 1/3 \text{tr} \boldsymbol{\epsilon} \mathbf{1}$  designates the strain deviator, and  $\Delta \mathbf{e}_{n+1}^p \equiv \mathbf{e}_{n+1}^p - \mathbf{e}_n^p$  the incremental plastic strain deviator. By assuming *linear isotropic* stress-elastic strain relations, and introducing the additive decomposition (2.1)<sub>1</sub>, the stress tensor at  $t_{n+1}$  may be expressed as

$$\begin{aligned} \boldsymbol{\sigma}_{n+1} &= K \text{tr} \boldsymbol{\epsilon}_{n+1}^e \mathbf{1} + 2G \mathbf{e}_{n+1}^e \\ &\equiv \boldsymbol{\sigma}^E - K \text{tr} \Delta \boldsymbol{\epsilon}_{n+1}^p \mathbf{1} - 2G \Delta \mathbf{e}_{n+1}^p \end{aligned} \quad (2.9)$$

where  $\boldsymbol{\sigma}^E$  is the so-called *elastic trial stress* or *elastic predictor* defined as:

$$\boldsymbol{\sigma}^E \equiv \boldsymbol{\sigma}_n + \left(K - \frac{2G}{3}\right) \text{tr} \Delta \boldsymbol{\epsilon}_{n+1} \mathbf{1} + 2G \Delta \boldsymbol{\epsilon}_{n+1} \quad (2.10)$$

Substitution of (2.8) into (2.9), yields

$$\boldsymbol{\sigma}_{n+1} - \boldsymbol{\sigma}^E = \Delta \lambda_{n+1} \left[ 3K \frac{dF_e}{dJ_1} \mathbf{1} - 2G \frac{\boldsymbol{s}}{2\sqrt{J_{2D}}} \right] \Big|_{n+1} \quad (2.11)$$

It remains to determine  $\Delta \lambda_{n+1}$  by enforcing the consistency condition at  $t_{n+1}$ , i.e.  $\phi(\boldsymbol{\sigma}_{n+1}) = 0$ . However, instead of imposing this condition exactly, the yield function  $\phi$  is linearized about the elastic predictor,  $\boldsymbol{\sigma}^E$ , to obtain

$$\phi(\boldsymbol{\sigma}_{n+1}) \approx \phi(\boldsymbol{\sigma}^E) + \left. \frac{\partial \phi}{\partial \boldsymbol{\sigma}} \right|_{J_1^E} : (\boldsymbol{\sigma}_{n+1} - \boldsymbol{\sigma}^E) = 0 \quad (2.12)$$

where  $J_1^E$  is the first invariant of the trial elastic stress given from (2.9) as

$$J_1^E = J_{1,n+1} + 3K \Delta \epsilon_{v,n+1}^p \quad (2.13)$$

Consistent with the linear expansion (2.12), the following first order approximation is introduced

$$\left. \frac{dF_e}{dJ_1} \right|_{J_{1,n+1}} \approx \left. \frac{dF_e}{dJ_1} \right|_{J_1^E} \quad (2.14)$$

By substituting of (2.11) and (2.14) into (2.12),  $\Delta\lambda_{n+1}$  can be solved for to obtain a *first order accurate* expression

$$\Delta\lambda_{n+1} = \frac{f^E}{\left[ 9K \left( \left. \frac{dF_e}{dJ_1} \right|_{J_1^E} \right)^2 + G \right] \Big|_{J_1^E}} \quad (2.15)$$

where

$$f^E \equiv \phi(\sigma^E) = \sqrt{J_{2D}^E} - F_e(J_1^E) \quad (2.16)$$

Finally, inserting (2.14) and (2.15) into (2.8)<sub>2</sub> and solving for  $\Delta\epsilon_v^p$  we obtain

$$\Delta\epsilon_v^p \Big|_{n+1} = -3f^E \left. \frac{dF_e}{dJ_1} \right|_{J_1^E} / \left[ 9K \left( \left. \frac{dF_e}{dJ_1} \right|_{J_1^E} \right)^2 + G \right] \Big|_{J_1^E} \quad (2.17)$$

Equations (2.15) and (2.17) are in agreement with the expressions obtained in Ref. [3] (see Eq. (33) and (34)). It then follows from the foregoing analysis that in the procedure advocated in Ref. [3] consistency is enforced on the basis of the *linearized* yield function about the elastic predictor  $\sigma^E$ . As a result of this *linear* approximation, the return path is normal to the tangent at  $\sigma^E$  and not the failure envelope at  $\sigma_{n+1}$ . Hence, in a strict sense, the normality condition is violated. A more fundamental lack of consistency arises in the treatment of the "singular corner region" in the vicinity of the intersection of cap and failure surface. This question is examined in some detail next.

### 2.3 Treatment of the singular corner region

In the following discussion, a stress state is envisioned as a point in the two dimensional stress space  $(J_1, \sqrt{J_{2D}})$ . In regard to the position of the elastic predictor,  $(J_1^E, \sqrt{J_{2D}^E})$ , two basic situations may arise.

*Case I* The elastic predictor falls in the corner region corresponding to the previous time step. That is

$$L(\kappa_n) - [\sqrt{J_{2D}^E} - F_e(L(\kappa_n))] \left. \frac{dF_e}{dJ_1} \right|_{J_1=L(\kappa_n)} < J_1^E < L(\kappa_n) \quad (2.18)$$

The procedure advocated in [3] then leads to a final value  $J_{1,n+1} > L(\kappa_n)$ , due to the use of a *linearized* normality rule, see Fig. 2. Since this violates the construction associated with the failure envelope mode, the solution proposed in [3] is simply to set  $J_{1,n+1} \equiv L(\kappa_n)$ , and  $\kappa_{n+1} \equiv \kappa_n$  (see Eq. (36) in [3]). We now show that this procedure results in open violation of the basic cap model behavior.



To see this we note that, since  $\kappa$  remains constant, the cap can neither contract nor expand. Due to the one-to-one correspondence between plastic volume change and hardening of the cap, it follows that *no plastic volume change* is allowed to take place; i.e.,  $\Delta\epsilon_v^p \equiv \text{tr } \epsilon^p = 0$ . However, Eq. (2.13), which connects changes in plastic volume and predicted as well as final values of  $J_1$ , must always hold

$$J_{1_{n+1}} \equiv J_1^E - 3K \Delta\epsilon_v^p \quad (2.19)$$

Thus, since  $\Delta\epsilon_v^p \equiv 0$  it follows that  $J_{1_{n+1}} \equiv J_1^E$  which is in manifest contradiction with the assumption that  $J_{1_{n+1}} = L(\kappa_n)$ .

*Case 2* Let us denote by  $(J_1^P, \sqrt{J_{2D}^P})$  the projection onto the failure surface,  $\sqrt{J_{2D}} - F_e = 0$ , of the elastic predictor. This case is concerned with the situation that  $[L(\kappa_n) - J_1^P]$  is *less than*  $[J_1^P - J_1^E]$ , see Fig. 3. Since there is a one-to-one correspondence between cap contraction and plastic volume change, in view of Eq. (2.19) the cap contraction must be large enough to satisfy

$$\Delta\epsilon_v^p = (J_1^E - J_1)/3K \quad (2.20)$$

It is clear, however, that for large enough values of  $[J_1^E - J_1]$  the difference between  $J_1^P$  and  $L(\kappa_n)$  may become too small to furnish the  $\Delta\epsilon_v^p$  required by (2.20). When this situation occurs, the procedure advocated in [3] (Eq. (37)), simply imposes  $\kappa_{n+1} \equiv J_1^P \equiv J_{1_{n+1}}$ . This treatment again violates Eq. (2.20).

### 3 Closest point projection algorithm. Inviscid case

In this section we show that, for the inviscid cap model, *exact* enforcement of the consistency condition,  $\phi(\sigma_{n+1}) = 0$ , reduces to a single scalar nonlinear equation involving the hardening parameter  $\kappa$ . In addition, the proper treatment of the singular corner region is also addressed.

#### 3.1 Formulation of the algorithm

To formulate the scalar nonlinear equation governing the consistency condition, we start by rephrasing Eq. (2.8)<sub>2</sub> in Section 2.2 as

$$\Delta\lambda_{n+1} = - \frac{\Delta\epsilon_v^p}{3\Omega} \Big|_{n+1} \quad (3.1)$$

where

$$\Omega_{n+1} \equiv \begin{cases} \frac{\partial F_c}{\partial J_1} \Big|_{J_{1_{n+1}}, \kappa_{n+1}} & (\text{cap mode}) \\ \frac{dF_e}{dJ_1} \Big|_{J_{1_{n+1}}} & (\text{failure mode}) \end{cases} \quad (3.2)$$

By definition we have

$$\Delta \mathbf{e}_{n+1}^p \equiv \Delta \boldsymbol{\epsilon}_{n+1}^p - \frac{1}{3} \Delta \epsilon_{v,n+1}^p \mathbf{1} \quad (3.3)$$

Substitution of (2.7),(3.1) and (3.2) into (3.3), yields

$$\Delta \mathbf{e}_{n+1}^p = - \frac{\mathbf{s} \Delta \epsilon_v^p}{6\Omega \sqrt{J_{2D}}} \Big|_{n+1} \quad (3.4)$$

In addition, from (2.9), we have the following relation between elastic predictor and final values

$$[\mathbf{s} + 2G \Delta \mathbf{e}_{n+1}^p] \Big|_{n+1} = \mathbf{s}^E \quad (3.5)$$

Combining (3.4) and (3.5), we obtain

$$\mathbf{s} \left[ 1 - \frac{G \Delta \epsilon_v^p}{3\Omega \sqrt{J_{2D}}} \right] \Big|_{n+1} = \mathbf{s}^E \quad (3.6)$$

After squaring (tensor contraction) both sides of (3.6) and taking the square root, we obtain the following governing equation

$$\boxed{\left[ \sqrt{J_{2D}} - \frac{G \Delta \epsilon_v^p}{3\Omega} \right] \Big|_{n+1} = \sqrt{J_{2D}^E}}$$

Consequently, it is seen that the closest point procedure reduces to the single nonlinear scalar equation (3.7) in terms of the hardening parameter  $\kappa$ . Since the derivative of (3.7) results in a rather cumbersome expression, an iterative procedure employing a secant method is employed in lieu of Newton's method.

**Remark 3.1** Eq. (3.7) is a scalar nonlinear equation. A secant-type scheme with super-linear rate of asymptotic convergence furnishes an economical solution procedure that avoids explicit evaluation of derivatives.  $\square$

**Remark 3.2** In the original cap algorithm, the derivative  $\Omega$  given by (3.2) is computed by a finite difference scheme. Here, the exact expression is used to evaluate  $\Omega$ .  $\square$

### 3.2 Consistent treatment of the singular corner region

The basic procedure for the consistent treatment of the singular corner region is essentially the same as the one discussed in detail in Section 3.1, and summarized in Box 1. The only crucial difference lies in the form taken by  $\Omega$ . From the discussion in Section 2.3 it is clear that for cases 1 and 2 the final value of  $J_1$  can neither coincide with the value at the corner point of previous time step, nor remain at the current elastic predictor value  $J_1^E$ . The final value  $J_1$  must lie between  $L(\kappa_n)$  and  $J_1^E$ ; i.e.,

$$J_1^E < J_1 < L(\kappa_n) \quad (3.8)$$

Appropriate satisfaction of the flow rule in the corner region then leads to the following expression for  $\Omega$  that replaces (3.2)<sub>2</sub>

$$\kappa_{n+1} = J_{1_{n+1}} \quad (\kappa_{n+1} \geq 0) \quad (3.9a)$$

$$\Omega_{n+1} = \frac{G}{9K} \frac{J_{1_{n+1}} - J_1^E}{\sqrt{J_{2D}^E} - F_e(J_{1_{n+1}})}$$

Equations (3.9a),(3.9b) together with (2.3),(2.13), and (3.7) furnish the consistent treatment of the singular corner region for the cases 1 and 2 discussed in Section 2.3. See Figures 2 and 3 for a geometric interpretation. Note that the elastic predictor falls within a new corner region where the vertex is the final stress point. A flowchart for the overall update procedure of the inviscid cap algorithm is listed in Box 1, where compression is taken to be positive.

**Remark 3.3** If the so-called *von Mises transition* is adopted in the cap algorithm when  $\kappa_{n+1} < 0$ , then Eq. (3.8) and (3.9) may be modified in the following fashion:

$$\kappa_{n+1} = 0, \quad \Delta \epsilon_v^p = \epsilon_v^p \Big|_{\kappa=0} - \epsilon_v^p \quad (3.10)$$

In addition,  $J_1, \sqrt{J_{2D}}$  are computed through Eq. (2.4) and (2.13).  $\square$

### 3.3 Accuracy analysis. Iso-error maps

The accuracy properties of the closest point algorithm are examined next. A precise assessment of accuracy for finite strain increments may be obtained by computing the iso-error contours. The initial and subsequent yield surfaces as well as various initial loading points are shown in Fig. 4. Figures 5-7 display the computed iso-error contours for the *inviscid* cap model under various loading conditions. The measure of numerical error (percentage) is defined as

$$ERROR \equiv 100 * \frac{\sqrt{(\sigma_{ij} - \sigma_{ij}^*)(\sigma_{ij} - \sigma_{ij}^*) + (\kappa - \kappa^*)^2}}{\sqrt{\sigma_{ij}^* \sigma_{ij}^* + \kappa^{*2}}} \quad (3.11)$$

where  $(\sigma_{ij}, \kappa), (\sigma_{ij}^*, \kappa^*)$  are the computed and exact values of stresses and hardening parameters, respectively. The value of the material parameters used in the computations are the following :  $K=2100 \text{ ksi}, G=1700 \text{ ksi}, \alpha=3.86 \text{ ksi}, \Theta=.11, \gamma=1.16 \text{ ksi}, \beta=.44 \text{ ksi}^{-1}, R=4.43, D=.0032 \text{ ksi}^{-1}, W=.42, X^o=16 \text{ ksi}$ . This choice of parameters represents the "Colorado concrete" data [16].

Fig. 5 is concerned with the case in which plastic loading takes place from the hydrostatic axis. It is seen that the magnitude of the numerical error remains within reasonable

**BOX 1. Inviscid Cap Model Algorithm**

(i) Strain update:

$$\boldsymbol{\epsilon}_{n+1} = \boldsymbol{\epsilon}_n + \Delta \boldsymbol{\epsilon}_{n+1}$$

(ii) Elastic predictor (trial elastic stress):

$$J_1^E = J_{1,n} + 3K \operatorname{tr} \Delta \boldsymbol{\epsilon}_{n+1} ; \quad \boldsymbol{s}^E = \boldsymbol{s}_n + 2G \Delta \boldsymbol{e}_{n+1}$$

$$\sqrt{J_{2D}^E} = \frac{1}{2} \boldsymbol{s}^E : \boldsymbol{s}^E ; \quad \kappa^E = \kappa_n$$

(iii) Check modes:

$$J_1^{\text{crit}} \equiv L(\kappa_n) - [\sqrt{J_{2D}^E} - F_e(L(\kappa_n))] \frac{9K}{G} \Omega_n$$

(a) Tension cutoff mode: if  $J_1^E \leq T$

$$\text{Set } J_{1,n+1} = T ; \quad \sqrt{J_{2D,n+1}} = 0 ; \quad \text{GO TO (v)}$$

(b) Cap mode: if  $J_1^E > L(\kappa_n)$  and  $\sqrt{J_{2D}^E} > F_c(J_1^E, \kappa_n)$

$$\text{Set } \Omega_{n+1} \equiv \frac{\partial F_c}{\partial J_1}(J_{1,n+1}, \kappa_{n+1}) ; \quad \text{GO TO (iv)}$$

(c) Failure mode: if  $T < J_1^E < J_1^{\text{crit}}$  and  $\sqrt{J_{2D}^E} > F_e(J_1^E)$

$$\text{Set } \Omega_{n+1} \equiv \frac{dF_e}{dJ_1}(J_{1,n+1}) ; \quad \text{GO TO (iv)}$$

If  $\kappa_{n+1} = J_{1,n+1}$ , set  $\Omega_{n+1}$  as in mode (d) next.

(d) Corner region: if  $J_1^{\text{crit}} < J_1^E < L(\kappa_n)$  and  $\sqrt{J_{2D}^E} > F_e(J_1^E)$

$$\text{Set } \kappa_{n+1} = J_{1,n+1} ; \quad \Omega_{n+1} = \frac{G}{9K} \frac{J_{1,n+1} - J_1^E}{\sqrt{J_{2D}^E} - F_e(J_{1,n+1})} ; \quad \text{GO TO (iv)}$$

(e) Elastic mode: if none of the above is invoked. Use elastic predictor.

$$\text{Set } J_{1,n+1} = J_1^E , \quad \sqrt{J_{2D,n+1}} = \sqrt{J_{2D}^E} ; \quad \text{GO TO (v)}$$

(iv) Plastic correction: for modes (b), (c), and (d)

Solve by local iteration:

$$\begin{cases} J_{1,n+1} + 3K \Delta \epsilon_{v,n+1}^p = J_1^E \\ \sqrt{J_{2D,n+1}} + G \Delta \lambda_{n+1} = \sqrt{J_{2D}^E} \end{cases}$$

where

$$\Delta \epsilon_{v,n+1}^p = \epsilon_v^p(\kappa_{n+1}) - \epsilon_v^p(\kappa_n) ; \quad \Delta \lambda_{n+1} = -\frac{\Delta \epsilon_{v,n+1}^p}{3\Omega_{n+1}}$$

(v) Stress update:

$$\boldsymbol{s}_{n+1} = \frac{\sqrt{J_{2D,n+1}}}{\sqrt{J_{2D}^E}} \boldsymbol{s}^E ; \quad \boldsymbol{\sigma}_{n+1} = \boldsymbol{s}_{n+1} + \frac{J_{1,n+1}}{3} \mathbf{1} ; \quad \text{EXIT}$$

bounds even for strain increments that are relatively large compared with characteristic strains at yielding. Similar behavior is observed when plastic loading takes place from the corner point (Fig. 6) or the intermediate point (Fig. 7).

As we indicated in the previous sections, the major difference between the consistent algorithm proposed here and the original algorithm in [3] concerns the return path in the failure envelope mode. To assess the difference, one needs to compare the corresponding iso-error maps in the failure mode. However, for large volumetric strain increments, the tension cutoff mode appears instead of failure modes. This is due to the construction of the tension cutoff procedure. Nevertheless, one can still obtain results for large deviatoric strain increments coupled with small volumetric strain increments, see Figures 8 and 9. The numerical error for the closest point procedure ranges from 0.3 to 10%, while that of the original cap algorithm ranges from 1 to 82%. The source of the largest error in the latter arises from the inconsistent treatment of the *singular corner region* previously discussed in Section 2.3. The good accuracy of the proposed closest point procedure is demonstrated.

#### 4. Viscoplastic ( *rate-dependent* ) extension

In this section, a rate-dependent extension of the basic cap model within the context of Perzyna type viscoplasticity is developed [8]. Numerical simulations exhibiting the basic behavior of the model will be considered in Section 5.

##### 4.1 Basic formulation and algorithm

Basic formulation of the viscoplastic cap model is similar to its inviscid counterpart. The inviscid failure envelope and cap surface now play the role of *loading* surfaces. In addition, one postulates an associative viscoplastic flow rule of the form

$$\dot{\epsilon}^{vp} = \lambda \langle \phi(f) \rangle \frac{\partial f}{\partial \sigma} \quad (4.1)$$

where  $\dot{\epsilon}^{vp}$  denotes the viscoplastic strain rate tensor and  $\lambda$  the fluidity parameter. The dimensionless scalar function  $\phi(f)$  represents the viscous flow function,  $f$  the viscoplastic loading function, and  $\langle \rangle$  the McAuley bracket. For the two-invariant constitutive model, two commonly assumed forms of viscoplastic flow function are:

$$\phi(f) = \left[ \frac{\sqrt{J_{2D}}}{F} - 1 \right]^N \quad (4.2a)$$

$$\phi(f) = \exp \left[ \frac{\sqrt{J_{2D}}}{F} - 1 \right]^N - 1 \quad (4.2b)$$

where  $N \in \mathbb{R}^+$  and for the cap model  $f$  is expressed as

$$f \equiv \sqrt{J_{2D}} - F \quad (4.3)$$

$$F \equiv \begin{cases} F_e & \text{failure surface} \\ F_c & \text{cap surface} \end{cases} \quad (4.4)$$

In parallel to the development of the inviscid cap model algorithm given in Section 3.1, we have the following equations under loading condition:

$$\lambda \Delta t \equiv \Delta \lambda = - \frac{\Delta \epsilon_v^{vp}}{3\Omega \langle \phi(f) \rangle} \quad (\text{similar to Eq. (3.1)}) \quad (4.5a)$$

$$\langle \phi(f) \rangle = - \frac{\Delta \epsilon_v^{vp}}{3\Omega \Delta \lambda} \quad (4.5b)$$

$$\sqrt{J_{2D}} = f + F \quad (f > 0 \text{ when loading}) \quad (4.6)$$

In the above expressions, the subscript  $n+1$  has been dropped for simplicity.

The return mapping algorithm summarized in Box 1 can be readily extended to accommodate rate-dependent viscoplastic behavior. For this purpose we note that in the viscous case the loading stress point is allowed to be outside the *static* yield surface  $\sqrt{J_{2D}} - F = 0$ ; i.e.,  $f > 0$  for rate-dependent behavior. The algorithmic implication is that relaxation towards the yield surface is not completed. The final position of the stress point on the loading surface is then determined by a condition that plays an analogous role to the consistency condition in the inviscid case. The basic algorithm in Box 1 still applies with the exception of step (iv), which is replaced by the procedure summarized in Box 2 below.

**BOX 2.** *Viscoplastic Correction for Modes (b), (c) and (d)*

Step (iv):  
Solve by local iteration:

$$\begin{cases} J_{1_{n+1}} + 3K \Delta \epsilon_{v_{n+1}}^{vp} = J_1^E \\ \sqrt{J_{2D_{n+1}}} + G \Delta \lambda_{n+1} = \sqrt{J_{2D}^E} \end{cases}$$

where

$$\Delta \lambda_{n+1} \equiv \lambda_{n+1} \Delta t = - \frac{\Delta \epsilon_{v_{n+1}}^{vp}}{3\Omega_{n+1} \langle \phi(f) \rangle}$$

$$\langle \phi(f) \rangle = - \frac{\Delta \epsilon_{v_{n+1}}^{vp}}{3\Omega_{n+1} \Delta \lambda_{n+1}}, \quad \Delta \epsilon_{v_{n+1}}^p = \epsilon_v^p(\kappa_{n+1}) - \epsilon_v^p(\kappa_n)$$

**Remark 4.1** Note that in the viscoplastic case the static yield surface lags behind the loading stress state. This could produce an "apparent" softening stress-strain behavior. However, this is in fact only a time-dependent phenomenon.  $\square$

**Remark 4.2** The algorithm presented above provides a unified treatment for both inviscid and rate-dependent cap models within the framework of the closest point procedure. Furthermore, the solution procedure requires only the solution of a single scalar equation. This is in contrast with the recent development of a viscoplastic cap model considered by Katona [13]. The approach advocated by Katona relies heavily on the implicit procedure developed by Hughes and Taylor [10], which involves the solution of a system of nonlinear equations for each iteration within a given time step. By contrast, the simplicity and economy of the present algorithm is noted.  $\square$

## 5. Parameter estimation and numerical simulations

In order to assess the capability of the two-invariant cap model in predicting response behavior for actual materials such as concrete, model parameters need to be estimated from available experimental data. In this section, a parameter estimation procedure and assessment of the predictive capability of the cap model are presented. This is followed by extensive numerical simulation of both the inviscid and rate-dependent models for concrete data.

### 5.1 Parameter estimation. Marquardt-Levenberg algorithm

It is characteristic of currently employed parameter estimation procedures for the cap model (see e.g. [17,18]) to fit *separately* the failure envelope, cap surface, and hardening parameters. Typically, asymptotic failure points from TE, TC, SS, CTC, CTE, RTE, RTC and PL† are used with a least-square fit procedure to estimate the failure parameters; whereas iso-plastic volumetric strain contours are employed to estimate the cap shape parameter  $R$ . The hardening parameters  $D$  and  $W$  are fitted from HC tests.‡ Although this procedure provides a parameter fitting inspired by the physical construction of the cap model, it has the following two major drawbacks: (a) a large amount (more than 20 tests) of conventional experimental data are required (e.g. CTC, CTE etc.), and (b) it is not possible to utilize some existing nonconventional experimental work; e.g., the results from the "Colorado" experimental program [16]. Hence, a more flexible and systematic parameter estimation procedure is needed. This is the objective of the following section.

**Optimization algorithm** The basic idea of the procedure advocated here is to regard the optimal fitting process for given experimental data as a least-square *constrained optimization* problem. In this context, the objective function  $\Pi: \mathbb{R}^N \rightarrow \mathbb{R}$  is simply the sum-of-squares error function defined as

$$\Pi(\Psi) \equiv \sum_{I=1}^N ||\sigma_I(\Psi, \epsilon_I) - \sigma_I^*||^2 \quad (5.1a)$$

where

$N$  : number of observations

$\sigma_I$  : stress response from constitutive model considered

$\sigma_I^*$  : observed stress response

$\Psi$  : parameter vector (in  $\mathbb{R}^7$  for cap model)

$I$  :  $I^{\text{th}}$  data point

---

† TE stands for triaxial extension, TC triaxial compression, SS simple shear, CTC conventional triaxial compression, CTE conventional triaxial extension, RTE reduced triaxial extension, RTC reduced triaxial compression, and PL proportional loading.

‡ HC represents hydrostatic compression test.

The constraints imposed on the optimization problem emanate from physical restrictions placed on the cap parameters. For example, for a physically meaningful model one should have  $\alpha > 0$ ,  $\gamma > 0$ ,  $\alpha > \gamma$ ,  $\theta > 0$ ,  $\beta > 0$ ,  $R > 0$ ,  $D > 0$ ,  $W > 0$ . These constraints define a *feasible domain*  $\Xi \subset \mathbb{R}^7$ , which is a *convex* polygon. The resulting constrained optimization problem is then expressed as

$$\text{Find : } \min \Pi(\Psi) \text{ subject to } \Psi \in \Xi \quad (5.1b)$$

There exists a wide variety of algorithms for solving the standard convex optimization problem (5.1b) (e.g., see [21] for a review). The algorithm employed here is the well-known *Marquardt-Levenberg* algorithm together with the *Armijo* step-size rule [19-20]. This algorithm is essentially a hybrid of Newton and steepest descent (gradient) methods. It combines the ability of the steepest descent method to converge from an initial guess, which may be outside the region of convergence of other methods, with the rapid convergence characteristics of Newton's method near the solution. The Marquardt-Levenberg algorithm can be summarized in the following form:

$$\Psi_{i+1} = \Psi_i + \lambda_i \mathbf{h}_i \quad (5.2)$$

$$\mathbf{h}_i = -[\mathbf{H}_i + \eta_i \mathbf{D}_i]^{-1} \nabla_i \Pi \quad (5.3)$$

$$\mathbf{H}_i = 2 \mathbf{Q}_i^T \mathbf{Q}_i \quad (\text{approx. Hessian}) \quad (5.4)$$

$$\mathbf{Q}_i = \frac{\partial \boldsymbol{\sigma}}{\partial \Psi_i} \quad (\text{sensitivity matrix}) \quad (5.5)$$

$$\eta_i = \text{Marquardt parameter}$$

$$\mathbf{D}_i = \text{diagonal matrix of } \mathbf{H}_i, \text{ or simply } \mathbf{I}$$

$$\lambda_i = \underset{\omega \in (0,1), k \in \mathbb{N}}{\text{argmin}} \left\{ \omega^k \mid \Psi_{i+1} \in \Xi, \Pi(\Psi_{i+1}) < \Pi(\Psi_i) \right\} \quad (5.6)$$

$$i = i^{\text{th}} \text{ iteration}$$

The algorithm summarized above can be systematically applied to any set of experimental data to obtain the optimal fit for the constitutive model under consideration in a least square sense.

*Error measurement* During the optimization process, a root-mean-square (RMS) type of error measurement is adopted. The optimization process is considered to reach its optimum when the RMS measure is minimized. The relevant measures are defined as follows:

$$\Delta_N \equiv \left[ \frac{\Pi}{N} \right]^{\frac{1}{2}} \quad (\text{RMS of error}) \quad (5.7)$$

$$\Gamma_N \equiv \left[ \sum_{j=1}^N \frac{||\boldsymbol{\sigma}_j^*||^2}{N} \right]^{\frac{1}{2}} \quad (\text{RMS of observed responses}) \quad (5.8)$$

$$\delta_N \equiv \frac{\Delta_N}{\Gamma_N} \quad (\text{normalized relative RMS error}) \quad (5.9)$$



**Remark 5.1** It is interesting to examine the sensitivity of the response under perturbations in cap model parameters. A finite difference sensitivity matrix  $\mathbf{Q}$  is defined in dimensionless form:

$$Q_{ij} = \frac{\Delta\sigma_i / \sigma_i}{\Delta\Psi_j / \Psi_j} \quad (5.10)$$

where  $\sigma_i$  is a stress component ( $i = 1, \dots, 6$ ) and  $\Psi_j$  is a parameter component ( $j = 1, \dots, 7$ ), respectively. A standard sensitivity analysis reveals that the response of the cap model is relatively insensitive to changes in the model parameters. By ordering the model parameters according to relative sensitivity in the response, one obtains in decreasing order of sensitivity

$$W \rightarrow D \rightarrow R \rightarrow \alpha \rightarrow \theta \rightarrow \gamma \rightarrow \beta \quad (5.11)$$

In summary, one obtains the following relative degree of sensitivity (from large to small):

$$\text{hardening parameters} \rightarrow \text{cap parameters} \rightarrow \text{failure parameters}$$

## 5.2 Inviscid case. "Colorado" concrete data

In this section, we first examine the consistency of the "Colorado concrete" data [16], next we estimate the model parameters by exercising the procedure described above, finally assess the predictive capability for the inviscid cap model.

*Colorado concrete data* This program on concrete was performed at the University of Colorado (1983) and is well-documented. The program consists of six major series of non-conventional multiaxial stress-strain curves. The total number of experiments is 67. The data are characterized by the following properties: (a) characteristic strength  $f'_c \approx 4$  KSI, (b) mean pressure  $\leq 8$  KSI (c) *truly triaxial* states of stress for concrete, (d) nonconventional complicated stress paths, and (e) quasi-static loading.

*Assessment of data consistency* Basically, the measures employed here are the same as those discussed in the previous section. For convenience, these measures are summarized as follows:

$$\Delta_N \equiv \left[ \sum_{I=1}^N \frac{||\Delta\epsilon_I||^2}{N} \right]^{\frac{1}{2}} \quad (\text{see}(5.7)) \quad (5.12)$$

$$\Gamma_N \equiv \left[ \sum_{I=1}^N \frac{||\epsilon_I^A||^2}{N} \right]^{\frac{1}{2}} \quad (\text{see}(5.8)) \quad (5.13)$$

$$\delta_N \equiv \frac{\Delta_N}{\Gamma_N} \quad (\text{see}(5.9)) \quad (5.14)$$

Here  $\epsilon_I^A$  refers to a strain measurement of test 'A'. An assessment of consistency for the "Colorado" concrete data may be obtained from the replicates of experiments available in the reported results [16]. The present analysis generally indicates reasonable consistency of the

data. However, some serious discrepancies between replicates are also observed. See Table 1 below.

**Table 1.** Consistency of the Colorado concrete data [16]

Tests	$\delta$ %	Major Path
1-1 & 1-10	13.5	CTC
1-4 & 1-7	31.1	TC
1-6 & 1-9	51.3	TE
2-3 & 2-4	9.6	SS
2-7 & 2-8	13.5	SS
3-1 & 3-2	244.3	Circular
3-3 & 3-4	47.2	Circular
3-10 & 3-11	92.9	Circular
4-1 & 4-2	10.9	Axisymmetric
4-6 & 4-7	54.2	Axisymmetric

*Model parameter estimation procedure* The actual data employed in the optimization process based on the Marquardt-Levenberg algorithm are obtained by arbitrarily selecting *one* test out of each of the six major series. Thus, a total number of 6 tests is used in the actual fit of the model. The quality of the fitting is satisfactory. Typical values of the RMS error found from back-prediction are  $\delta = 16\%$  for test 1-1 (CTC),  $\delta = 8.5\%$  for test 2-3 (SS), etc.. From this optimization procedure, we obtain the following set of parameters which best fits the observed experiments:  $\alpha = 3.86 \text{ ksi}$ ,  $\theta = .11$ ,  $\gamma = 1.16 \text{ ksi}$ ,  $\beta = .44 \text{ ksi}^{-1}$ ,  $R = 4.43$ ,  $D = .0032 \text{ ksi}^{-1}$ ,  $W = .42$ ,  $X^o = 16 \text{ ksi}$ .

*Predictive capability* After the optimal model parameters are obtained, the resulting cap model is used to predict the response of *every* other Colorado test which is not included in the optimization process (total number = 61). It is emphasized that the "prediction" here has nothing to do with optimal fitting, but is obtained by exercising the cap model using previously estimated parameters. In general, considering the experimental data scatter, the predicted response is in good agreement with the experimental results. Values of the RMS error corresponding to a selected sample of simulations are summarized in Table 2 below. The overall RMS and standard deviation of error for 61 tests are 26.6% and 14%, respectively. A comparison between experimental and predicted stress-strain curves is contained in Figures 10-19.

*Assessment and evaluation* From the above fitting and prediction exercises, it may be concluded that for the Colorado concrete data the inviscid cap model generally exhibits good fitting and predictive capabilities. The simulations reported herein capture the *overall* qualitative behavior of the experimental response.

**Table 2. Results of prediction. Inviscid case**

Tests	$\delta$ %	Major Path
1-2	12.4	SS
1-3	14.1	TE
2-2	17.	TE
2-4	11.7	SS
3-5	15.	Circular
3-17	11.6	Circular
4-7	14.	Axisymmetric
4-12	11.4	Axisymmetric
5-1	14.	Unsymmetric
5-2	17.	Unsymmetric

### 5.3. Some rate-dependent simulations

Unlike the static tests, there are only limited amount of dynamic (high rate) tests available for concrete materials. In this section, simulations with the rate-dependent model are performed on the basis of two recent dynamic concrete tests. These preliminary simulations appear to substantiate the good fitting capabilities of the viscoplastic cap model. As in the inviscid case, the model parameters are identified by the optimization procedure discussed in Section 5.1, based on a modified Marquardt-Levenberg algorithm.

*SRI Dynamic Concrete Test (1979)* [14] First, the elastic bulk modulus  $K$  and shear modulus  $G$  are independently determined to be  $K=2100\text{ ksi}$ ,  $G=1700\text{ ksi}$ . By using the optimization algorithm, the cap model parameters are identified to be:  $\alpha=0.7\text{ ksi}$ ,  $\theta=0.1$ ,  $\gamma=0.2\text{ ksi}$ ,  $\beta=1.473\text{ ksi}^{-1}$ ,  $R=10.8$ ,  $D=0.00154\text{ ksi}^{-1}$ ,  $W=0.884$ ,  $X^o=18\text{ ksi}$  (the initial cap surface location),  $N=1.62$ , and  $\lambda=0.0000142\text{ sec}^{-1}$ . The error  $\delta$  obtained by the viscoplastic cap model, based on the above parameters, is only 4.8% , see Fig. 20. The correlation between the model's performance and the experimental data is quite satisfactory.

*TerraTek Research Dynamic Concrete Test #32 (1984)* [15] This test is concerned with a concrete material composed of limestone coarse aggregate, with sample size of 4-in diameter and 4-in length. The elastic parameters are independently determined to be:  $K=3571.43\text{ ksi}$ ,  $G=2459\text{ ksi}$ . Within the reliable testing region, the model parameters are identified to be:  $\alpha=2.1\text{ ksi}$ ,  $\theta=0.116$ ,  $\gamma=1.3\text{ ksi}$ ,  $\beta=0.3\text{ ksi}^{-1}$ ,  $R=9.7$ ,  $D=0.006\text{ ksi}^{-1}$ ,  $W=0.2$ ,  $X^o=56\text{ ksi}$ ,  $N=1.61$ , and  $\lambda=0.00036\text{ sec}^{-1}$ . The error  $\delta$  obtained by the viscoplastic cap model, based on the above parameters, is only 3% within the reliable experimental region, see Fig. 21.

The good agreement between predicted and experimental response for the two preliminary examples considered above appears to confirm the suitability of the viscoplastic model proposed in the present work for modeling rate-dependent behavior in concrete materials.

## 6. Closure

The algorithmic implementation of the cap model has been considered in detail. An existing stress point algorithm for the numerical integration of the inviscid cap model has been reviewed, and shown to be in conflict with the basic constitutive equations governing the response of the model. This inconsistency applies to the failure envelope model and is particularly important in the singular cone whose vertex is the intersection of cap and failure surfaces. An alternative closest point algorithm for the *inviscid* cap model, which is free from these shortcomings, has been proposed. Its accuracy has been precisely assessed by means of iso-error maps for the "Colorado concrete" data. It is concluded that the numerical error of the proposed algorithm remains reasonable even for relatively large strain increments.

To account for *rate-dependent* behavior, a viscoplastic extension of the basic cap model has been developed based on the notion of viscoplastic behavior as proposed by Perzyna. An efficient algorithm for this rate-dependent model has been developed, which, as opposed to popular existing methods, only requires the solution of a scalar nonlinear equation. The good predicting capabilities of the model have been demonstrated in two dynamic experimental tests of concrete furnished by SRI and TerraTek.

A systematic estimation procedure for the parameters involved in the cap model to given experimental data has been developed, based on a modified Marquardt-Levenberg optimization algorithm. This procedure has been applied to the extensive experimental program carried out at the University of Colorado and reported in [16]. It is emphasized that due to the *nonconventional* character of this experimental data, standard fitting procedures (e.g., Desai [17,18]) based on conventional tests can not be employed. The numerical simulations performed on the basis of these data support the good predictive capabilities of the cap model for concrete materials.

## Acknowledgement

This work was sponsored by the Defense Nuclear Agency under Contract No. DNA001-84-C-0304 with the University of California, Berkeley. This support and the interest and comments of Dr. Eugene Sevin are gratefully acknowledged.

## References

- [1] DiMaggio, F. L., and Sandler, I. S., "Material Models for Granular Soils," *J. of Engng Mech.*, A.S.C.E., 1971, pp. 935-950.
- [2] Sandler, I. S., DiMaggio, F. L., and Baladi, G. Y., "Generalized CAP Model for Geological Materials," *J. of the Geotech. Engng Div.*, A.S.C.E., Vol. 102, No. GT7, July, 1976, pp. 683-699.

- [3] Sandler, I. S., and Rubin, D., "An Algorithm and a Modular Subroutine for the Cap Model," *Int'l J. for Numer. and Analy. Meth. in Geomech.*, Vol. 3, 1979, pp. 173-186.
- [4] Ortiz, M., and Pinsky, P. M., "Global Analysis Methods for the Solution of Elastoplastic and Viscoplastic Dynamic Problems," *Report UCB/SESM 81/08*, Dept. Civil Engng., Univ. of Calif., Berkeley, 1981.
- [5] Simo, J. C., and Ortiz, M. "A Unified Approach to Finite Deformation Elastoplastic Analysis Based on the Use of Hyperelastic Constitutive Equations," *Comp. Meth. Appl. Mech. Engng*, 1984.
- [6] Ortiz, M., and Simo, J. C., "An Analysis of a New Class of Integration Algorithms for Elastoplastic Constitutive Relations," Brown University, Division of Engineering, 1984.
- [7] Wilkins, M. L., "Calculation of Elastic-Plastic Flow," in B. Alder et. al. (eds.), *Methods of Computational Physics, 3*, Academic Press, 1964.
- [8] Perzyna, P., "Fundamental Problems in Viscoplasticity," *Advances in Applied Mechanics*, Vol. 9, 1966, pp. 244-368.
- [9] Zienkiewicz, O. C., and Corneau, I. C., "Visco-Plasticity, Plasticity and Creep in Elastic Solids--A Unified Numerical Approach," *Int'l J. for Numer. Meth. in Engng*, Vol. 8, pp. 821-845.
- [10] Hughes, T. J. R., and Taylor, R. L., "Unconditionally Stable Algorithm for Quasi-Static Elasto/Viscoplastic Finite Element Analysis," *Computer and Structures*, Vol. 8, 1978, pp. 169-173.
- [11] Pinsky, P. M., Ortiz, M., and Pister, K. S., "Numerical Integration of Rate Constitutive Equations in Finite Deformation Analysis," *Comp. Meth. Appl. Mech. Engng.*, Vol. 40, 1983.
- [12] Simo, J. C., Hjelmstad, K. J., and Taylor, R. L., "Numerical Formulations for Elasto-Viscoplastic Beams Account for the Effect of Transverse Shear," *Comp. Meth. Appl. Mech. Engng.*, 1983.
- [13] Katona, M. G., "Evaluation of Viscoplastic Cap Model," *J. of Geotech. Engng.*, A.S.C.E., Vol. 110, No. 8, 1984, pp. 1106-1125.
- [14] Levine, H., "Concrete Modeling Using The Three-Invariant Cap," Weidlinger Associates, *DNA Concrete Meeting*, April 1985, Utah.
- [15] Bakhtar, K., et. al., "Concrete Material Properties," TerraTek Research, *DNA Concrete Meeting*, April 1985, Utah.
- [16] Scavuzzo, R., Stankowski, T., Gerstle, K. H., and Ko, H. Y., "Stress-Strain Curves for Concrete Under Multiaxial Load Histories," NSF CME-80-01508, Department of Civil Engineering, University of Colorado, Boulder, August 1983.
- [17] Desai, C. S., and Siriwardane, H. J., "Constitutive Laws for Engineering Materials", Prentice Hall, 1984.

- [18] Zaman, M. M., Desai, C. S., and Faruque, M. O., "An Algorithm for Determining Parameters for Cap Model from Raw Laboratory Test Data", *Proc. 4th Int. Conf. Numer. Meth. Geomech.*, Edmonton, Canada, 1982.
- [19] Marquardt, D. W., "An Algorithm for Least-Squares Estimation of Nonlinear Parameters", *Journal SIAM*, Vol. 11, No. 2, June 1963, pp. 431-441.
- [20] Levenberg, K., "A Method for the Solution of Certain Non-linear Problems in Least Squares", *Quart. Appl. Math.*, Vol. 2, 1944, pp. 164-168.
- [21] Luenberger, David G., "Introduction to Linear and Nonlinear Programming", 2nd edition, Addison-Wesley, 1984.

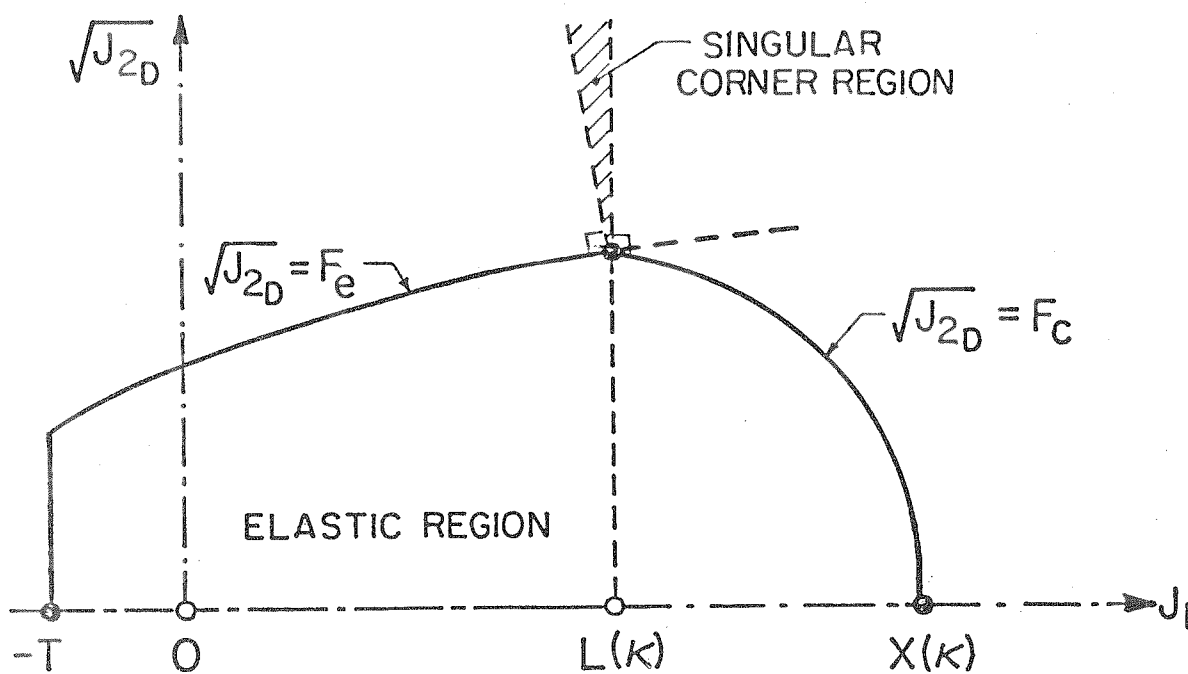


Figure 1. The yield surface for cap model.  $F_e$  and  $F_c$  denote the failure envelope and the hardening cap surface, respectively. The shaded area is the "singular corner region".

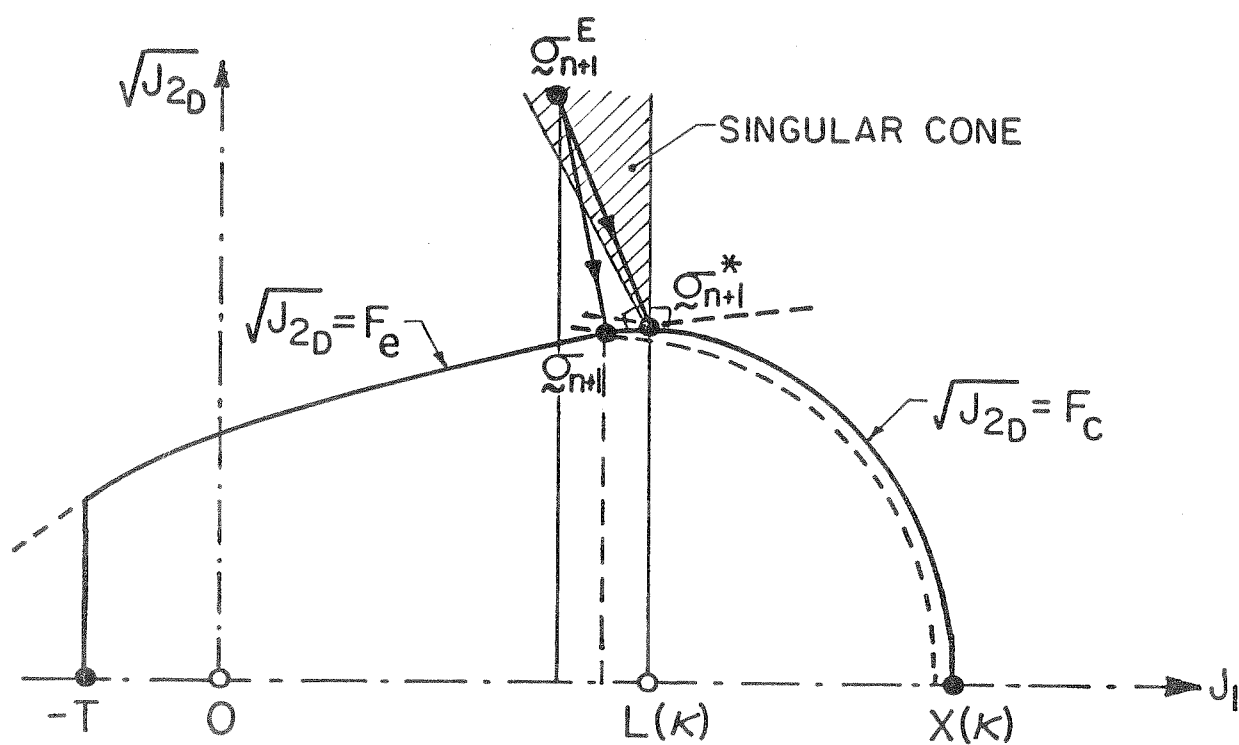


Figure 2. Case 1 of the singular corner mode. The elastic predictor falls in the corner region corresponding to the previous time step.  $\sigma_{n+1}^E$  signifies the elastic predictor, while  $\sigma_{n+1}^*$  represents the improper return stress point proposed in [3]. Note that  $\sigma_{n+1}$  is the correct return mapping point.



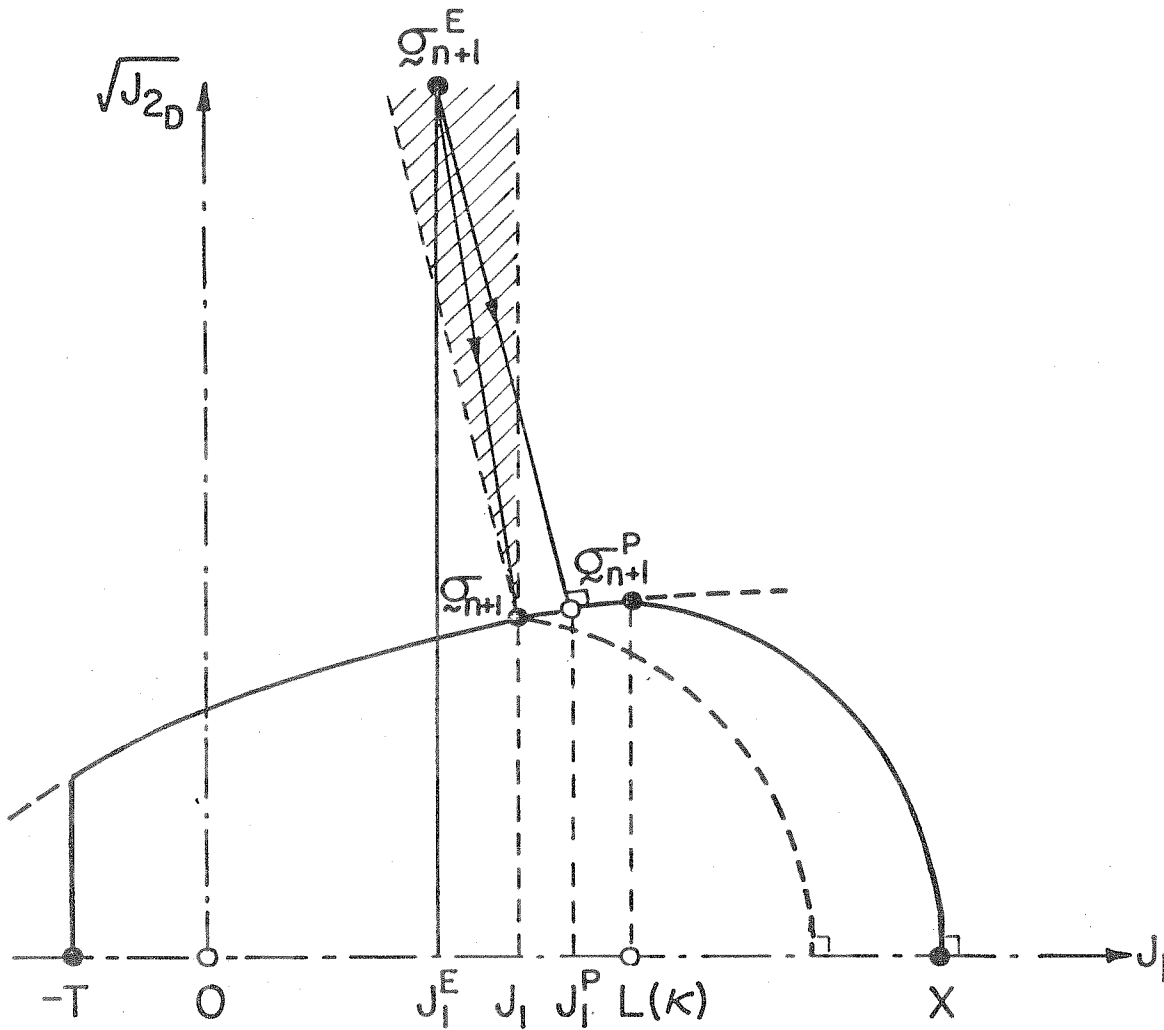


Figure 3. Case 2 of singular corner mode. The contraction of the cap catches up the return stress point on  $F_e$ . Note that  $\sigma_{n+1}^P$  is the orthogonal projection of  $\sigma_{n+1}^E$  on  $F_e$ . The correct return stress point is  $\sigma_{n+1}$ , i.e.  $J_1 = \kappa$ . Note that  $\sigma_{n+1}$  is the vertex of the newly formed corner region which contains the elastic predictor  $\sigma_{n+1}^E$ .

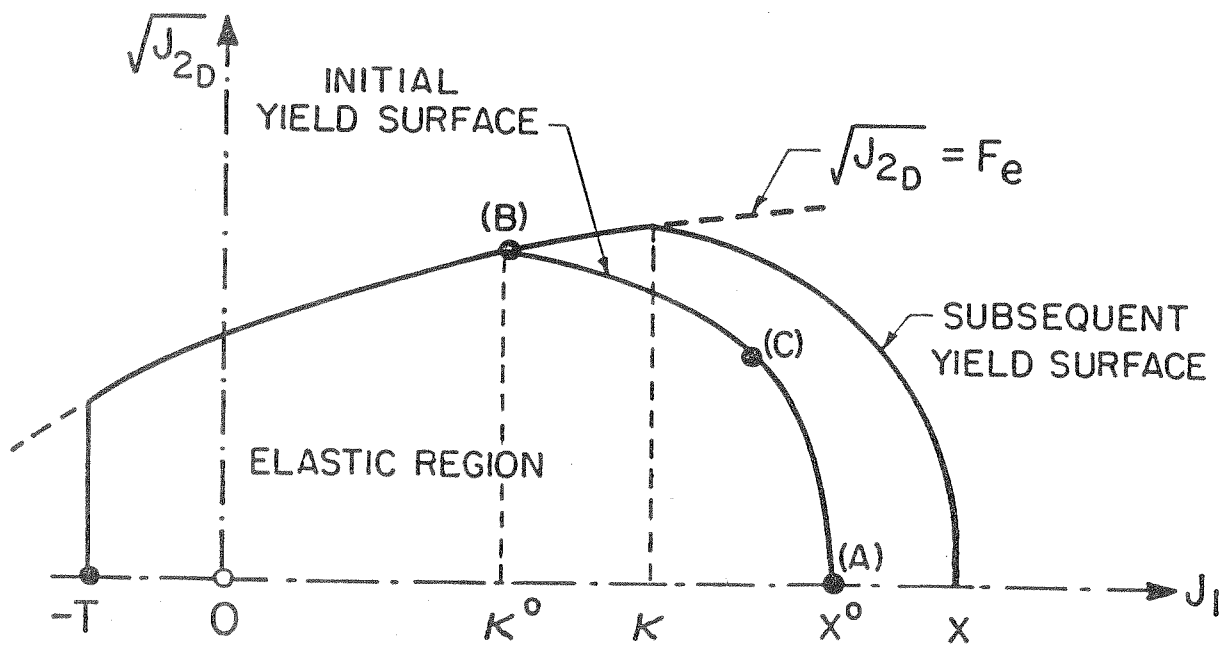


Figure 4. The initial and subsequent yield surfaces. Points (A), (B), and (C) represent three different initial loading points on the initial yield surface.

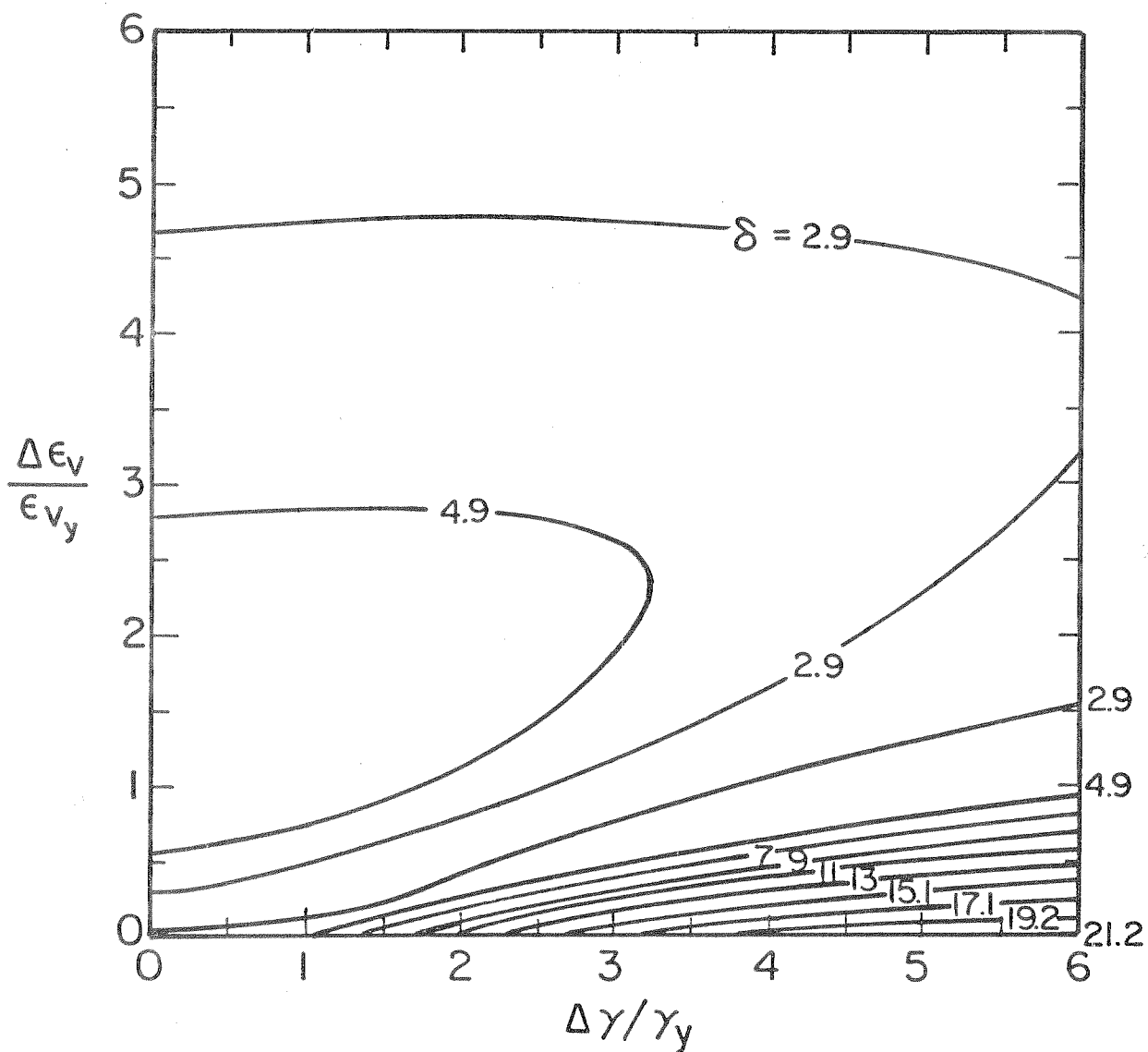


Figure 5. Percent iso-error contour for the closest point algorithm with compressive loading from the hydrostatic axis, point (A) in Fig. 4. The characteristic yield strains are defined as :  $\epsilon_{v_y} = \frac{x^o}{3K}$  and  $\gamma_y = \frac{\tau_y}{G}$ , where  $x^o$  is the initial cap position on  $J_1$ -axis and  $\tau_y$  the shear yield stress. Errors are shown for increasing volumetric and shear strain increments  $\Delta \epsilon_v$  and  $\Delta \gamma$ .

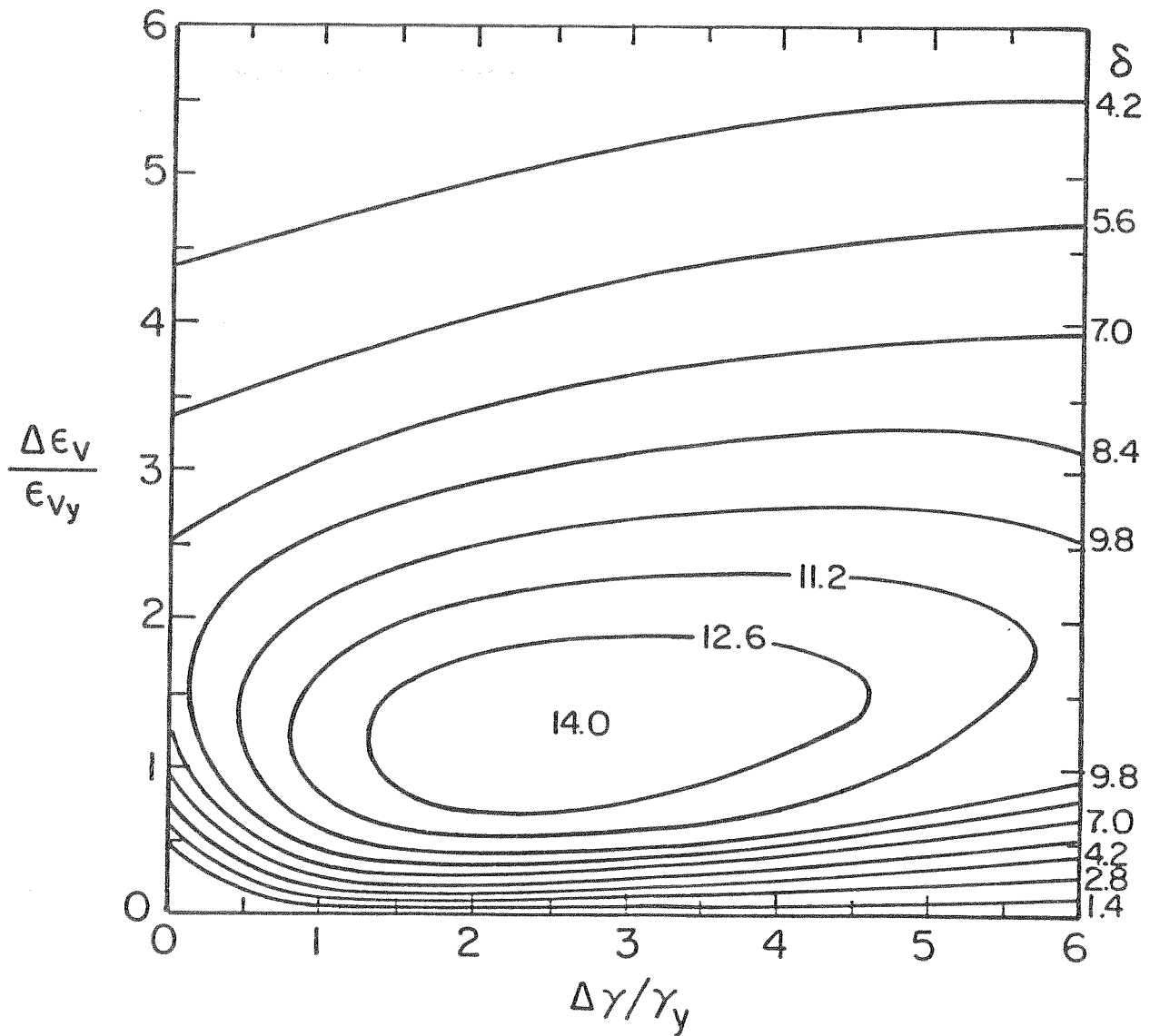


Figure 6. Percent iso-error contour for the closest point algorithm with compressive loading from the corner point (B), Fig. 4.

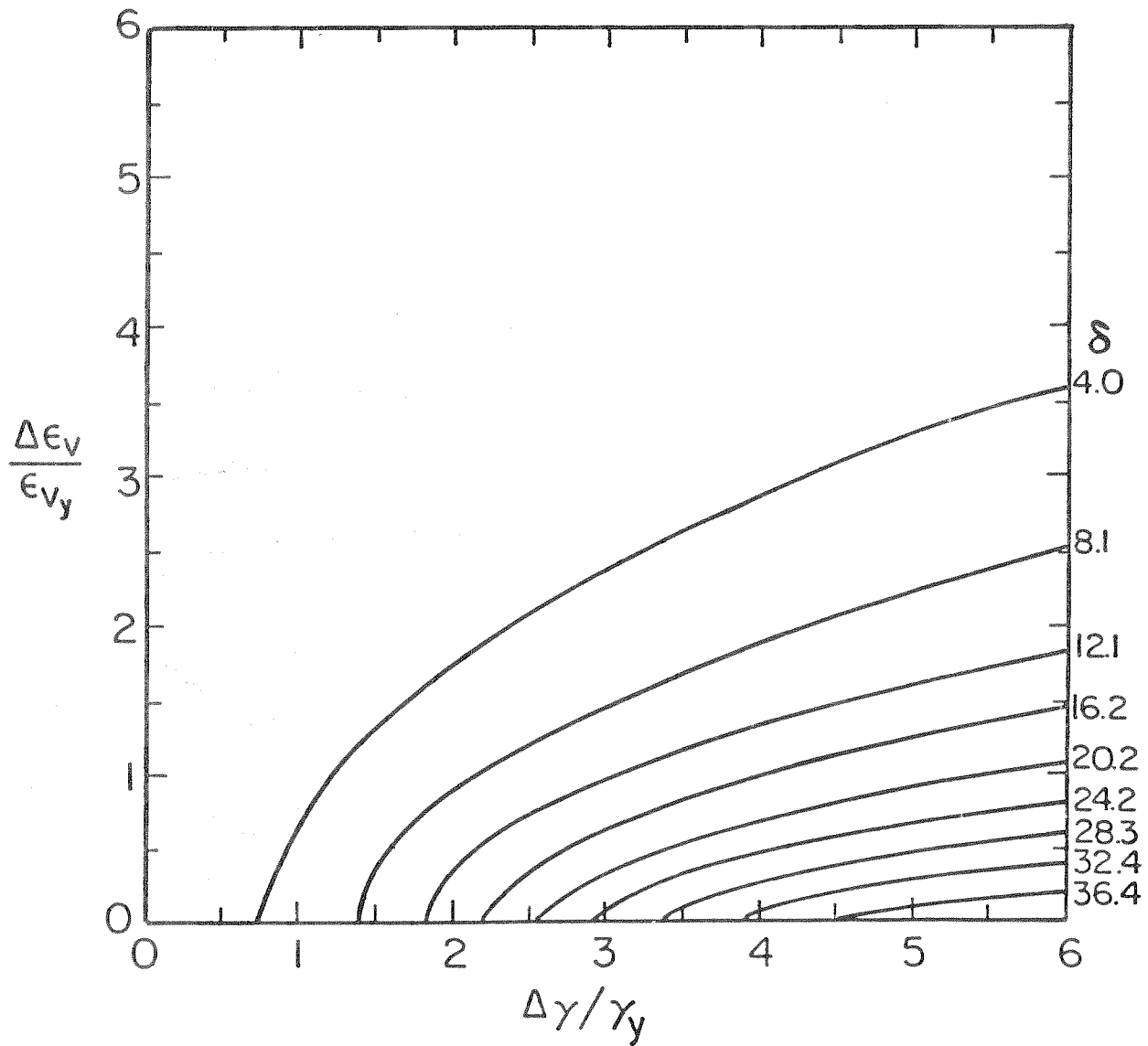


Figure 7. Percent iso-error contour for the closest point algorithm with compressive loading from the intermediate point (C), Fig. 4.

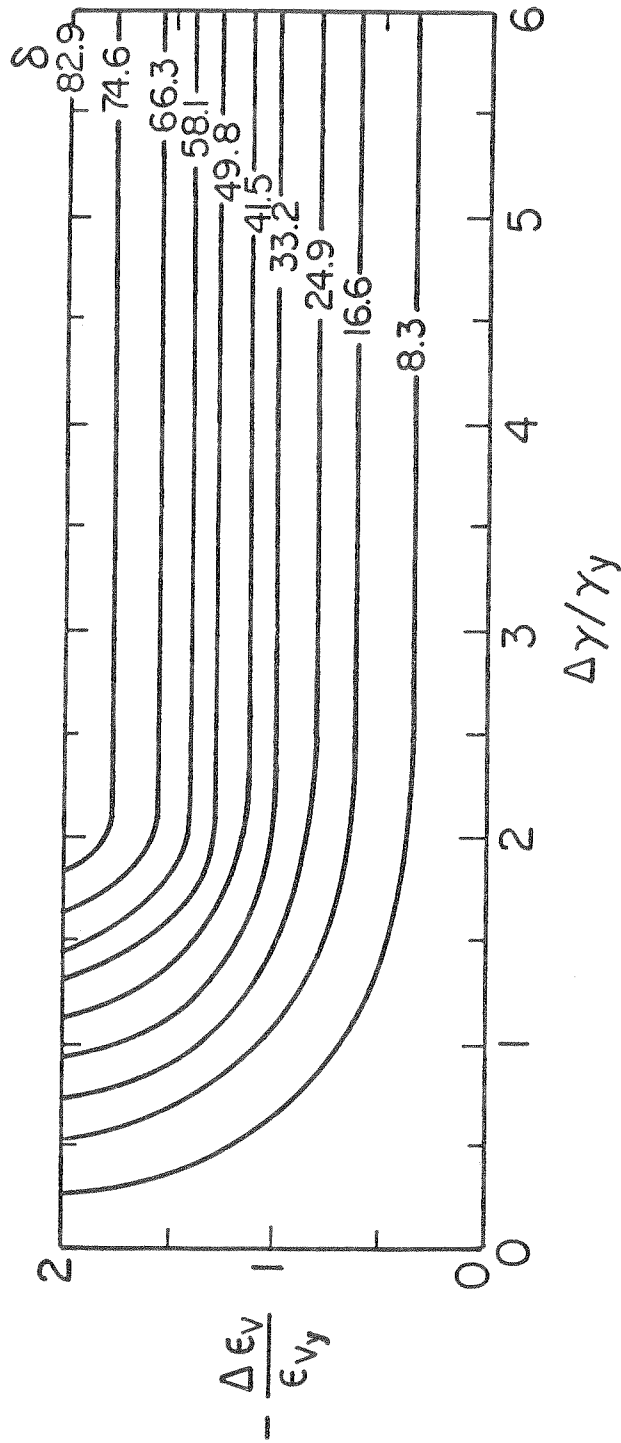


Figure 8. Percent iso-error contour for the original cap algorithm with tensile loading from the corner point (B), Fig. 4.

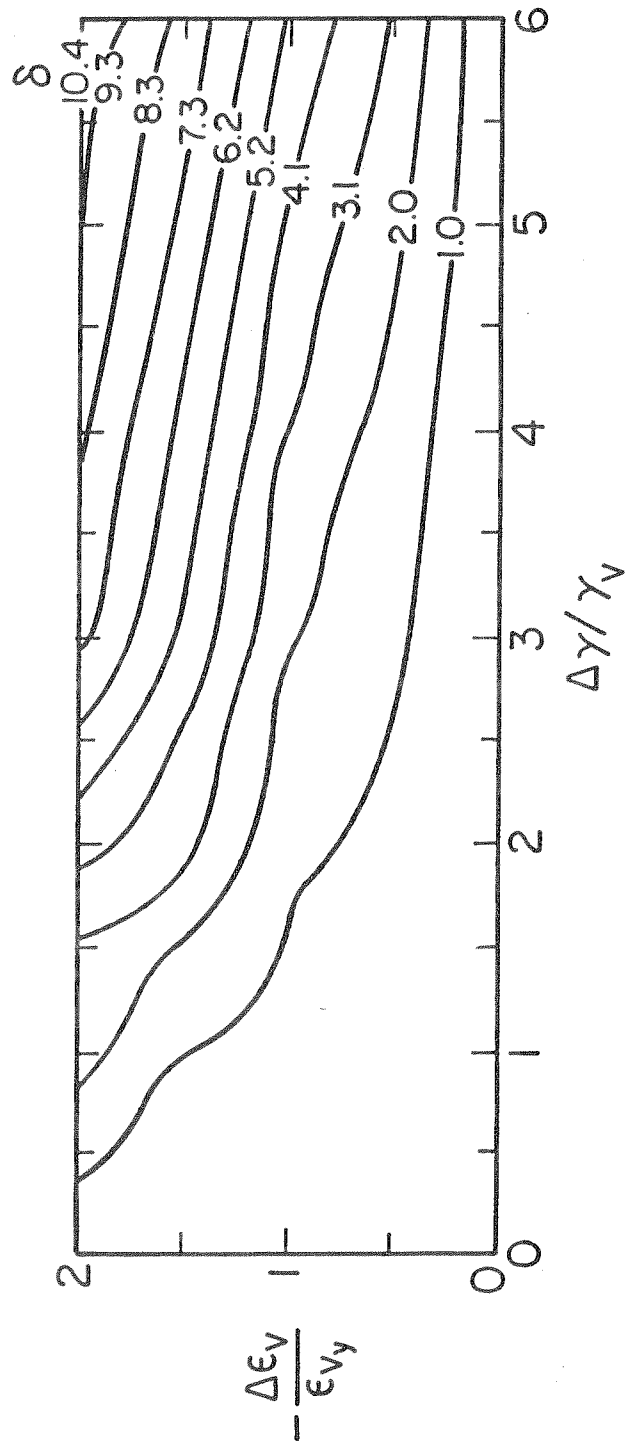


Figure 9. Percent iso-error contour for the closest point algorithm with tensile loading from the corner point (B), Fig. 4.

COMPARISON OF EXPERI. & SIMUL. DATA FOR CONCRETE TEST 1-2

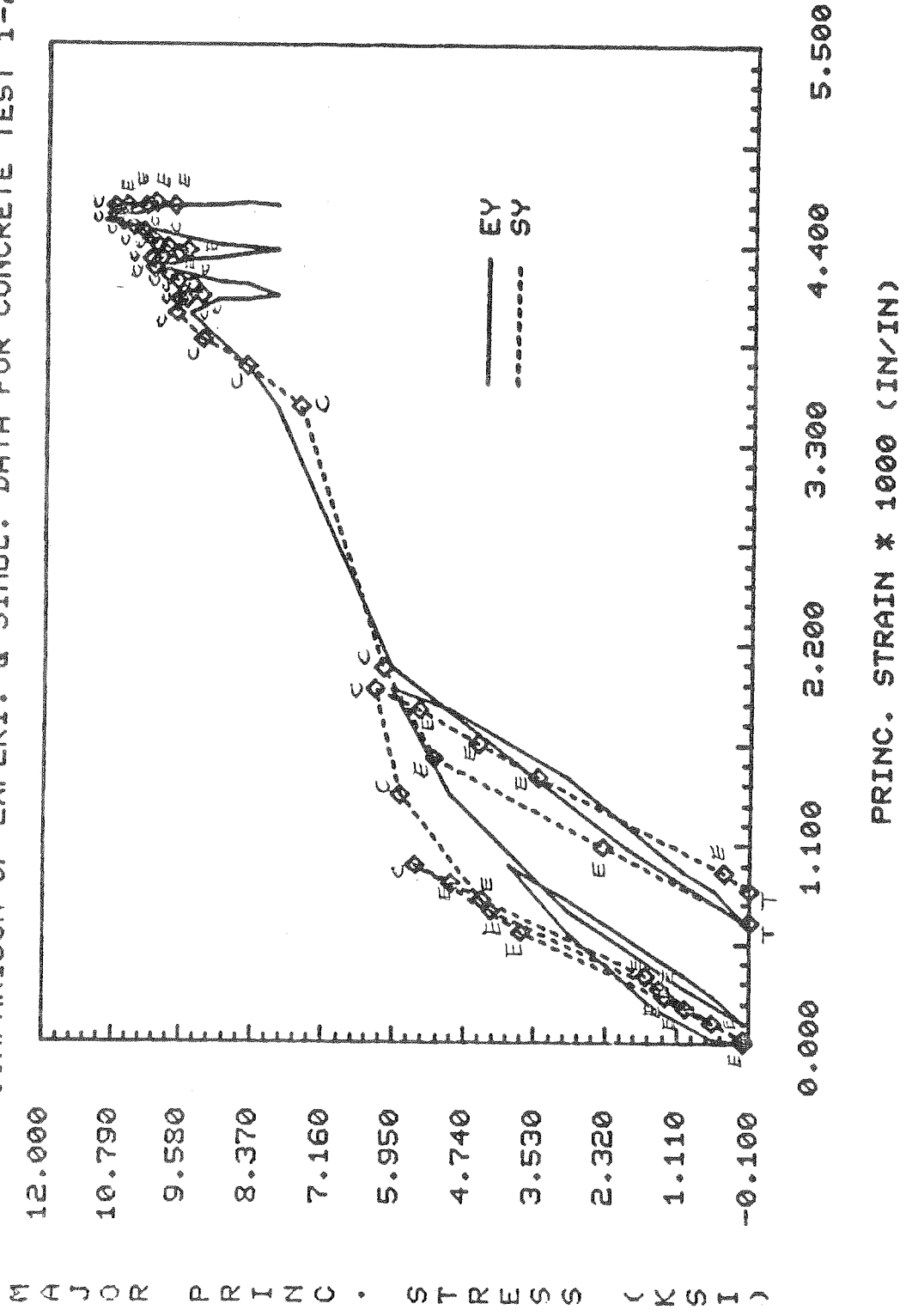


Figure 10. Comparison of the experimental and simulated data for concrete test 1-2. This is a cyclic simple shear test. The vertical axis is the major principal stress and the horizontal axis is one of the three principal strains. "EY" (solid-line) and "SY" (dash-line) represent the experimental and the simulated response in Y-direction, respectively. The diamond symbols signify the data points along "SY", in which "E" stands for the elastic mode, "C" for the cap mode and "T" for the tension cutoff mode. The r.m.s. error measure  $\delta = 12.4\%$ .



COMPARISON OF EXPERI. & SIMUL. DATA FOR CONCRETE TEST 1-3

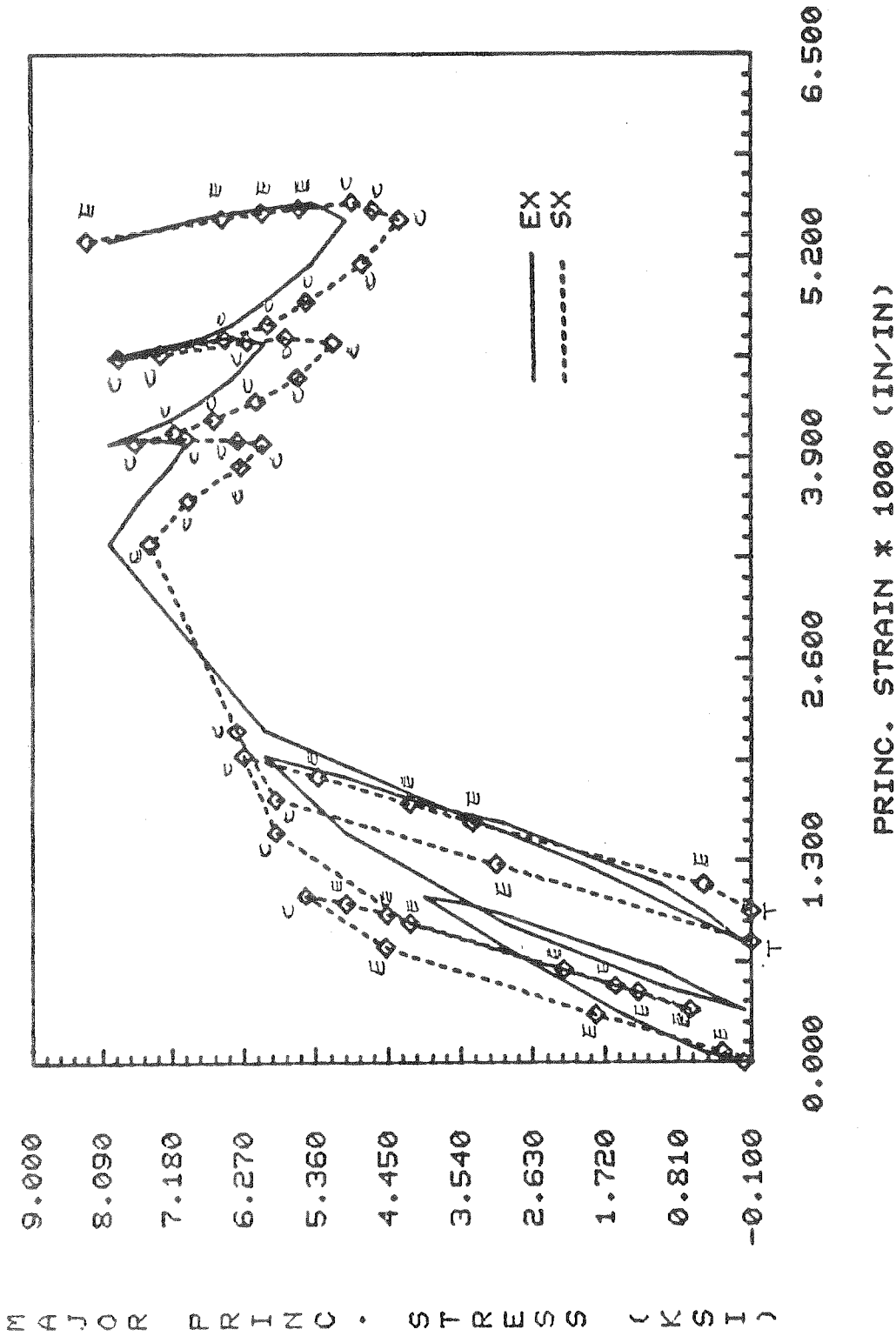


Figure 11. Comparison of the experimental and simulated data for concrete test 1-3. This is a cyclic triaxial extension test. The vertical axis is the major principal stress and the horizontal axis is one of the three principal strains. "EX" and "SX" represent the experimental and the simulated response in X-direction, respectively. The r.m.s. error measure  $\delta = 14.1\%$ .

COMPARISON OF EXPERI. & SIMUL. DATA FOR CONCRETE TEST 2-2

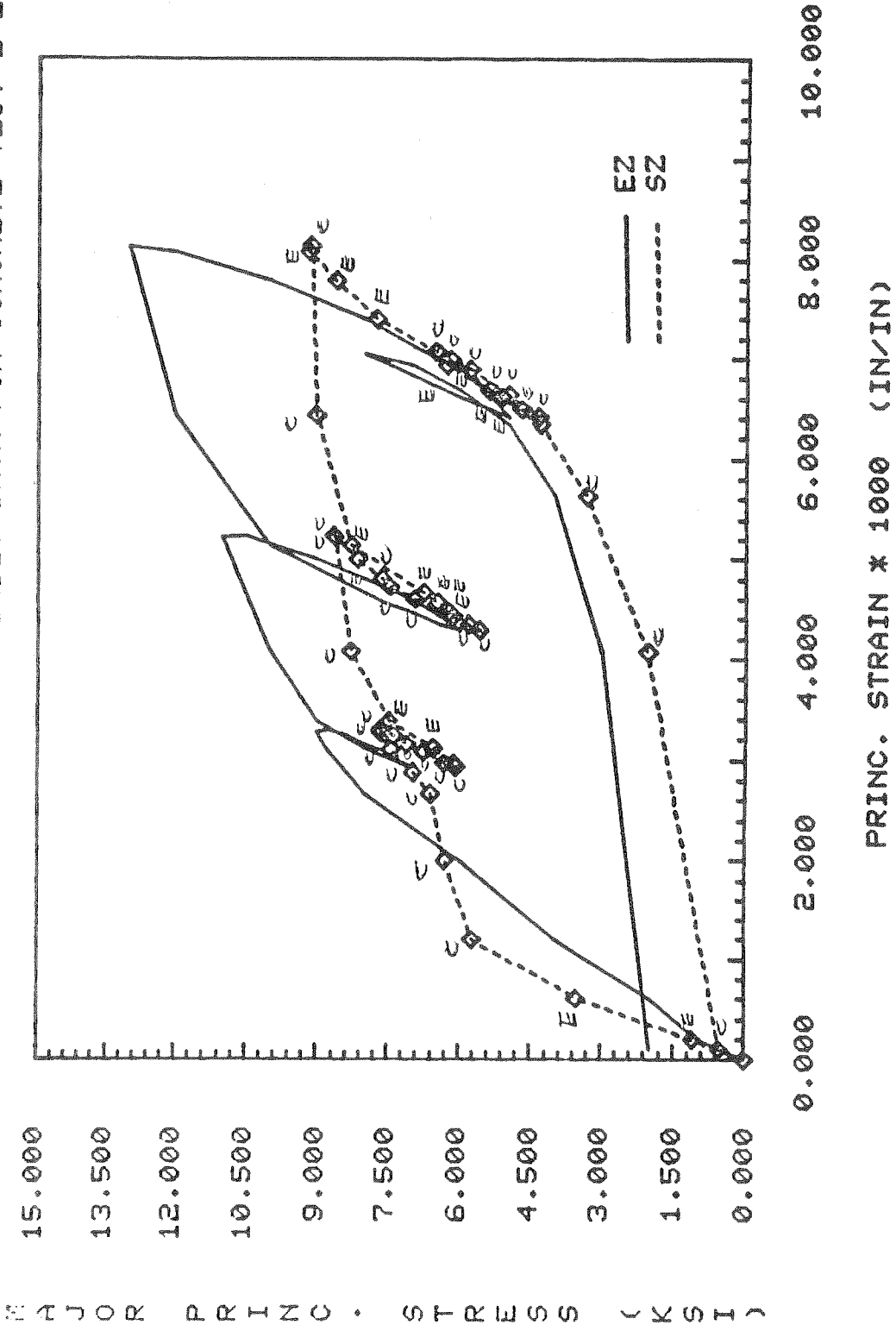


Figure 12. Comparison of the experimental and simulated data for concrete test 2-2. This is a cyclic triaxial extension test with stress reversal about the hydrostatic axis. "EZ" and "SZ" represent the experimental and the simulated response in Z-direction, respectively. The r.m.s. error measure  $\delta = 17\%$ .

COMPARISON OF EXPERI. & SIMUL. DATA FOR CONCRETE TEST 2-4

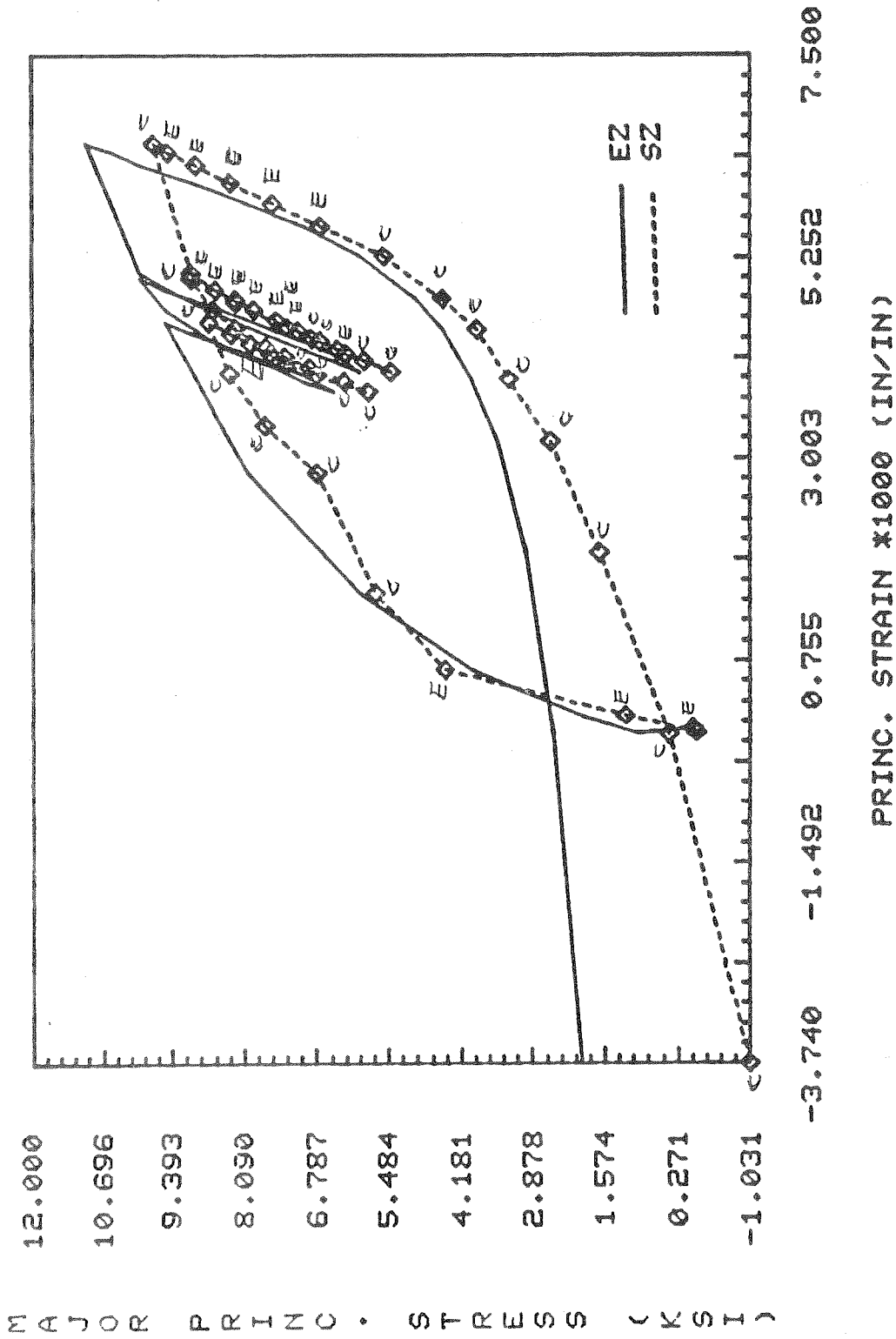


Figure 13. Comparison of the experimental and simulated data for concrete test 2-4. This is a cyclic simple shear test with stress reversal with respect to the hydrostatic axis. See Fig. 12 for the meaning of "EZ" and "SZ". The r.m.s. error measure  $\delta = 11.7\%$ .

COMPARISON OF EXPERI. & SIMUL. DATA FOR CONCRETE TEST 3-5

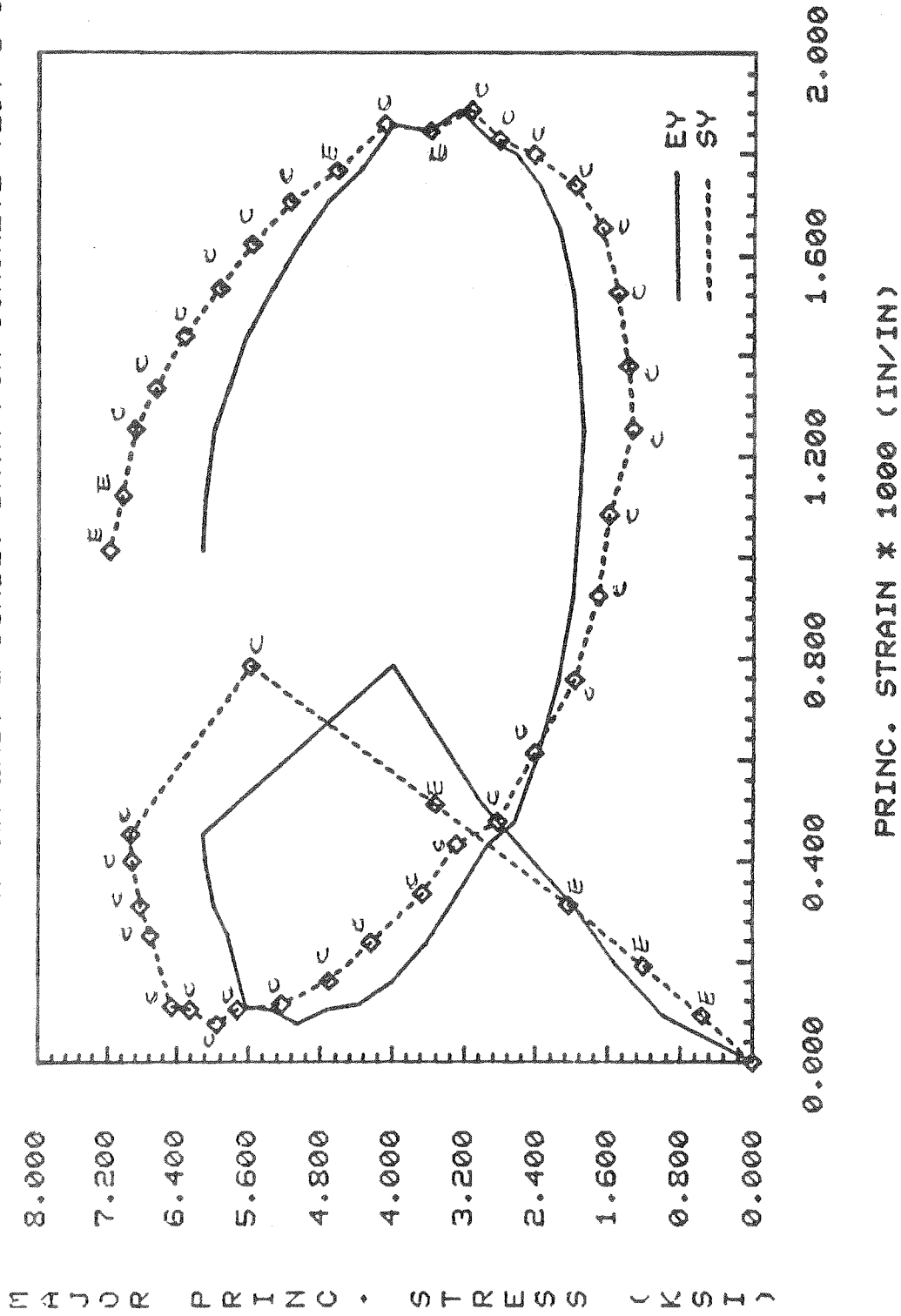


Figure 14. Comparison of the experimental and simulated data for concrete test 3-5. This is a circular stress path on the 12 KSI octahedral plane. See Fig. 10 for the meaning of "EY" and "SY". The r.m.s. error measure  $\delta = 15\%$ .

COMPARISON OF EXPERI. & SIMUL. DATA FOR CONCRETE TEST 3-17

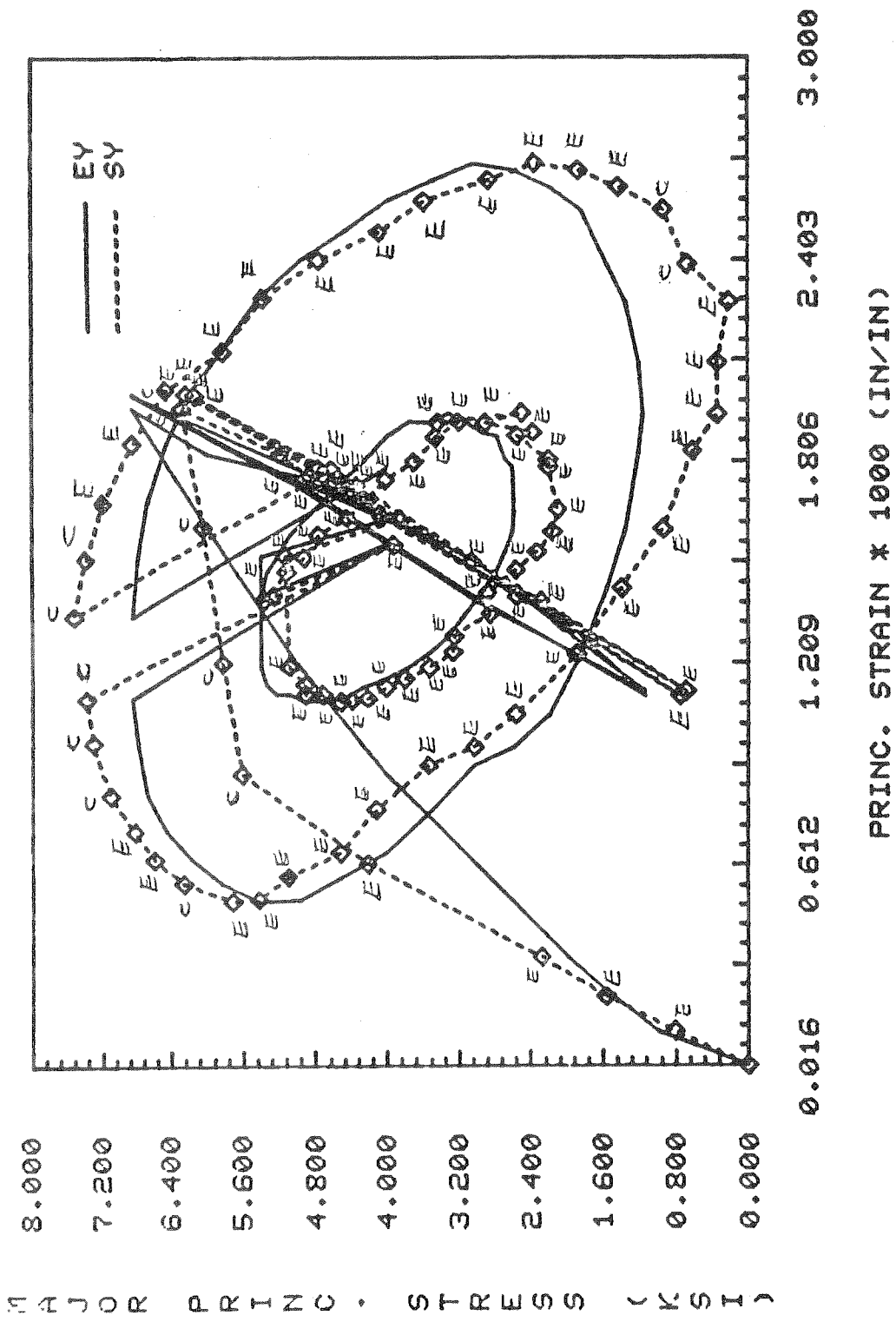


Figure 15. Comparison of the experimental and simulated data for concrete test 3-17. This is a proportional loading path followed by cyclic circular stress path on two octahedral planes, and finally followed by another proportional loading path. The r.m.s. error measure  $\delta = 11.6\%$ .

COMPARISON OF EXPERI. & SIMUL. DATA FOR CONCRETE TEST 4-7

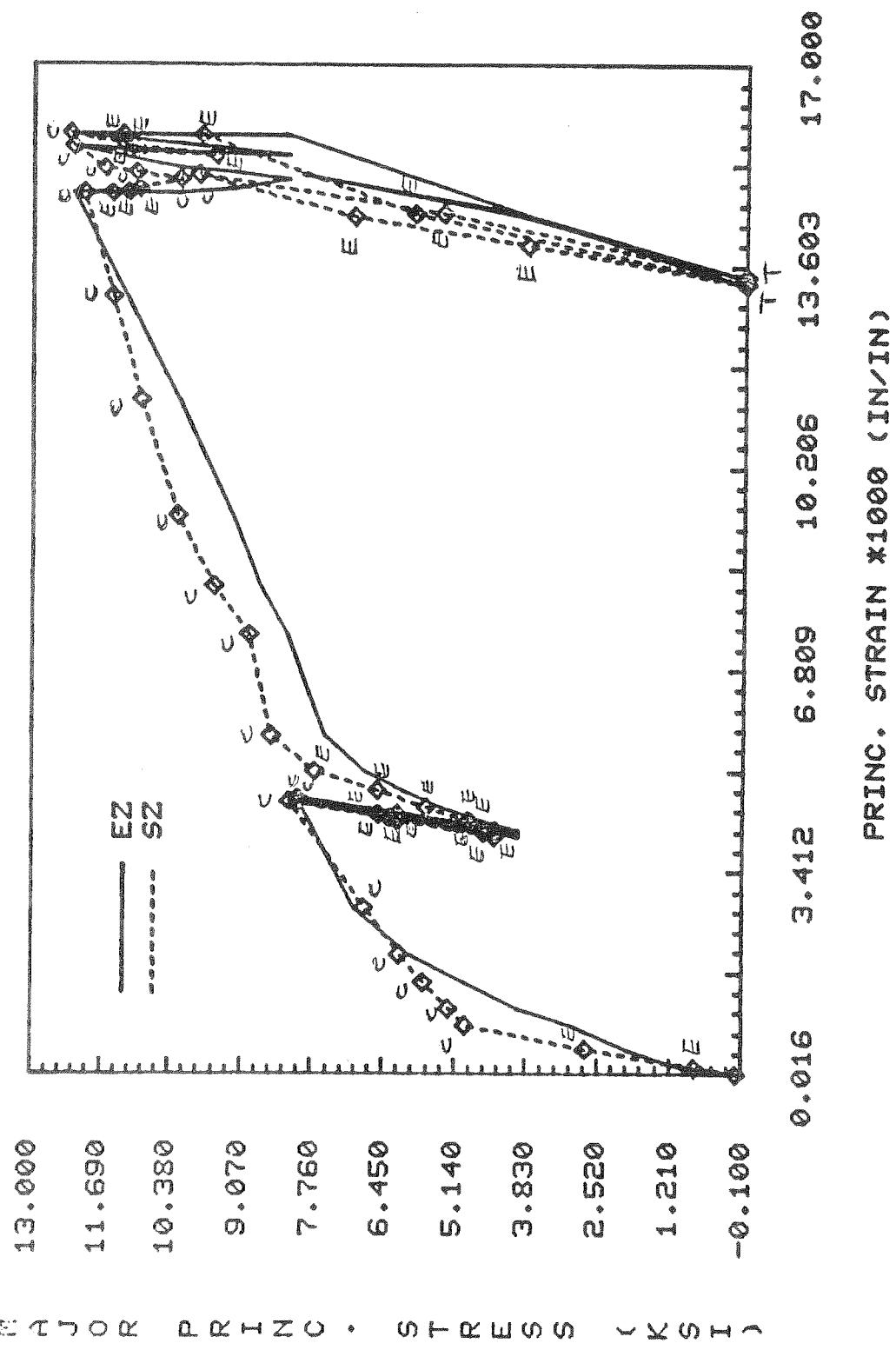


Figure 16. Comparison of the experimental and simulated data for concrete test 4-7. This is a cyclic axisymmetric triaxial compression test. The r.m.s. error measure  $\delta = 14\%$ .

COMPARISON OF EXPERI. & SIMUL. DATA FOR CONCRETE TEST 4-12

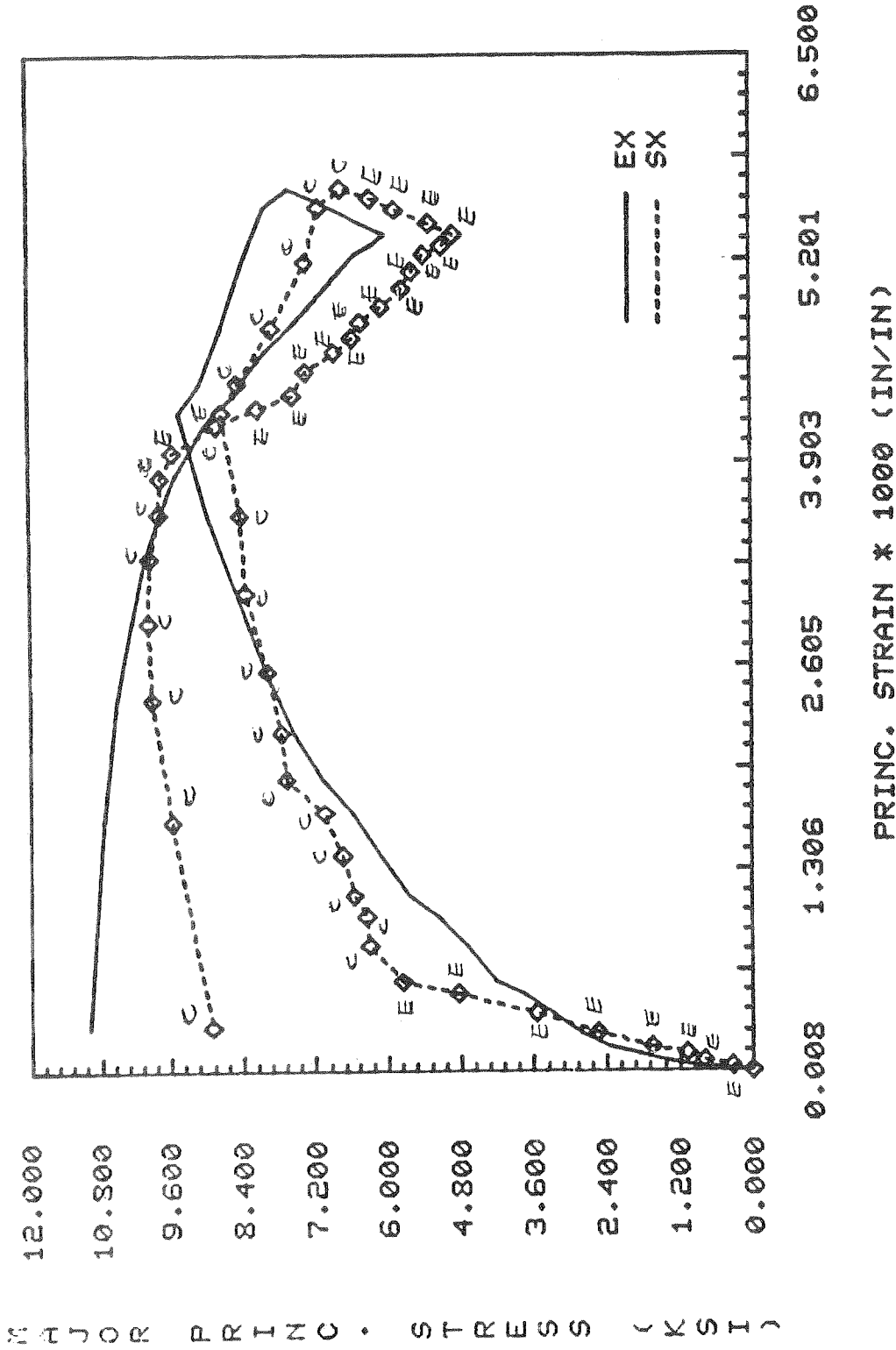


Figure 17. Comparison of the experimental and simulated data for concrete test 4-12. This is another cyclic axisymmetric triaxial test. See Fig. 11 for the meaning of "EX" and "SX". The r.m.s. error measure  $\delta = 11.4\%$ .

COMPARISON OF EXPERI. & SIMUL. DATA FOR CONCRETE TEST 5-1

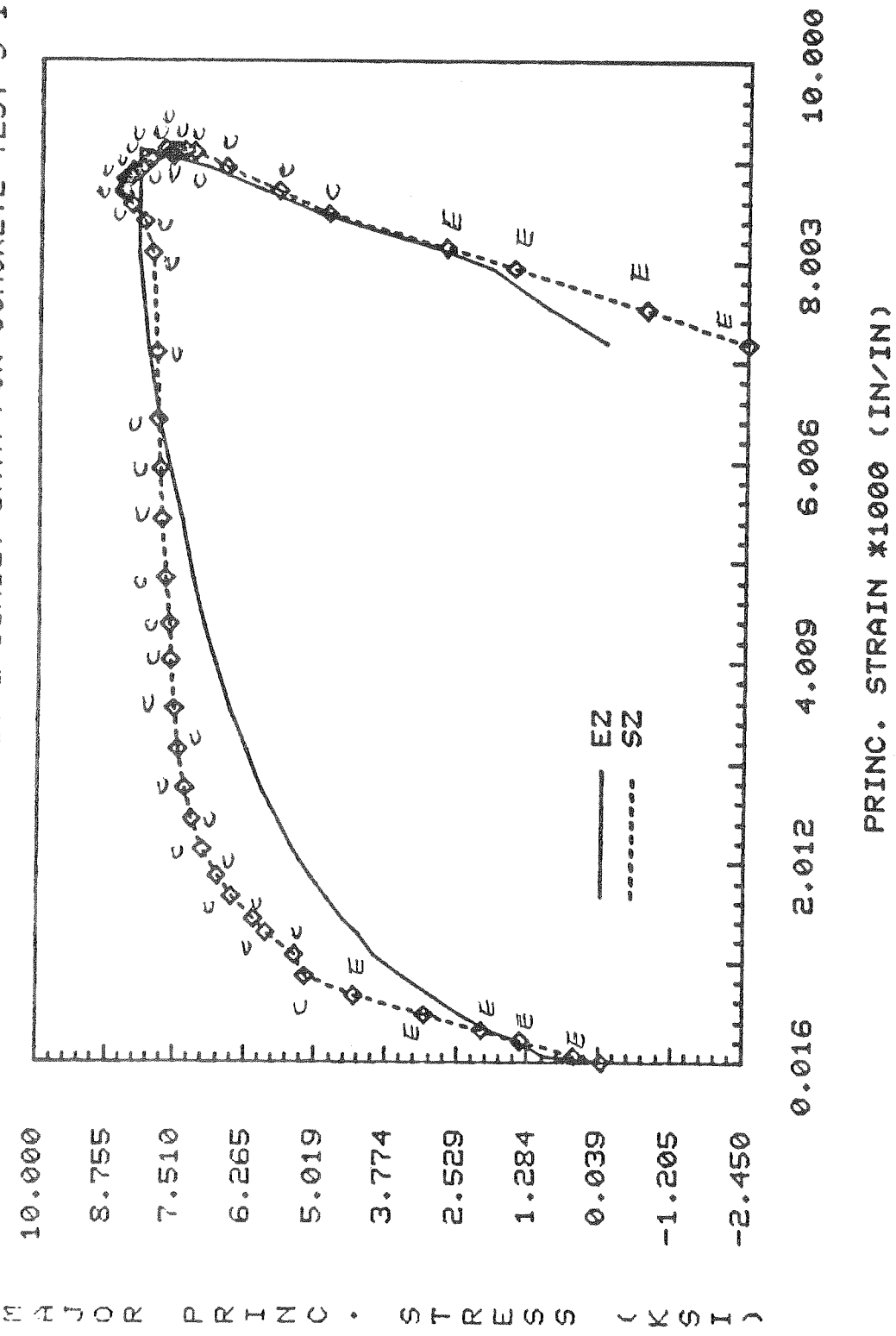


Figure 18. Comparison of the experimental and simulated data for concrete test 5-1. This is an unsymmetric triaxial test. The r.m.s. error measure  $\delta = 1.4\%$ .



COMPARISON OF EXPERI. & SIMUL. DATA FOR CONCRETE TEST 5-2

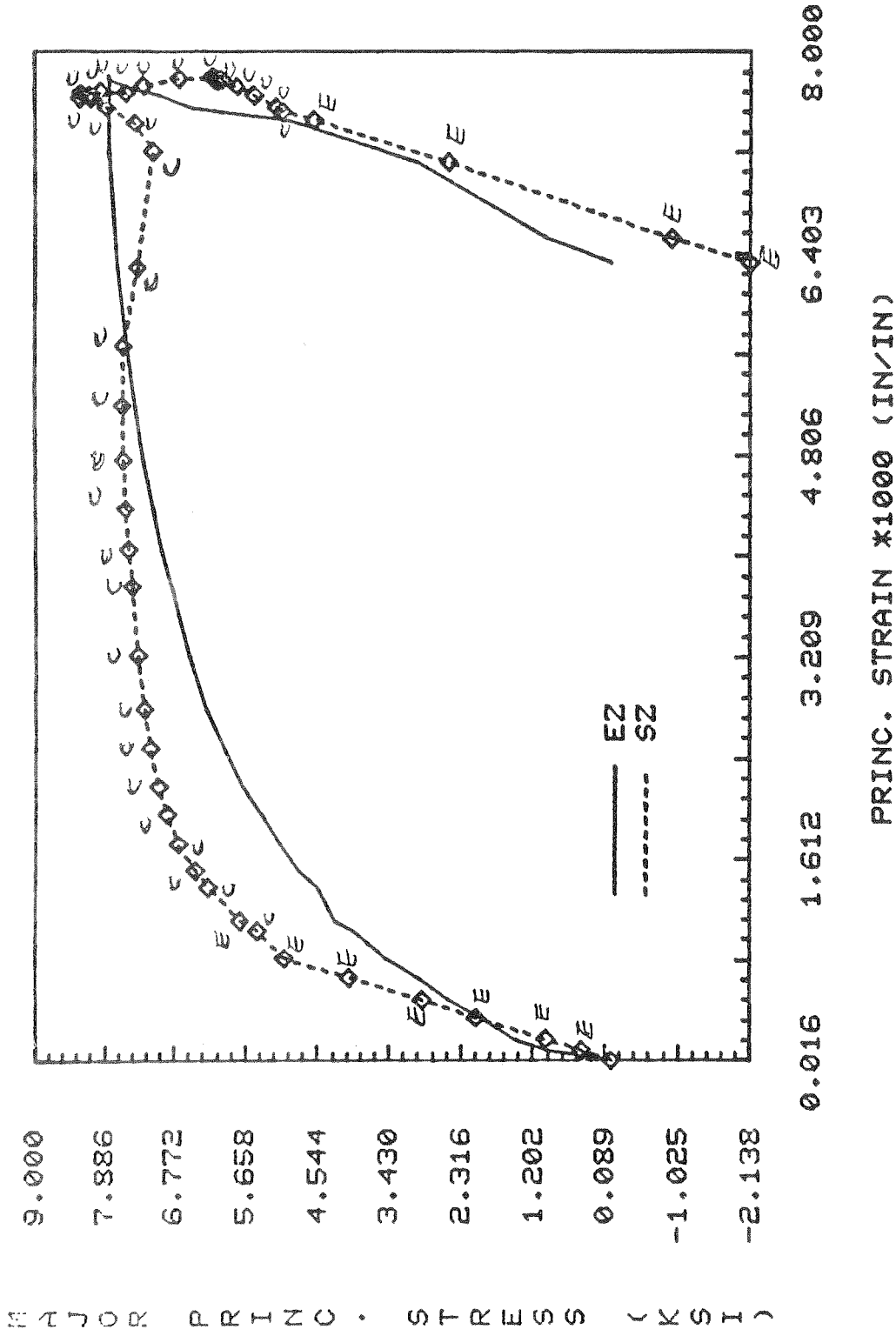


Figure 19. Comparison of the experimental and simulated data for concrete test 5-2. This is an unsymmetric triaxial test. The r.m.s. error measure  $\delta = 17\%$ .

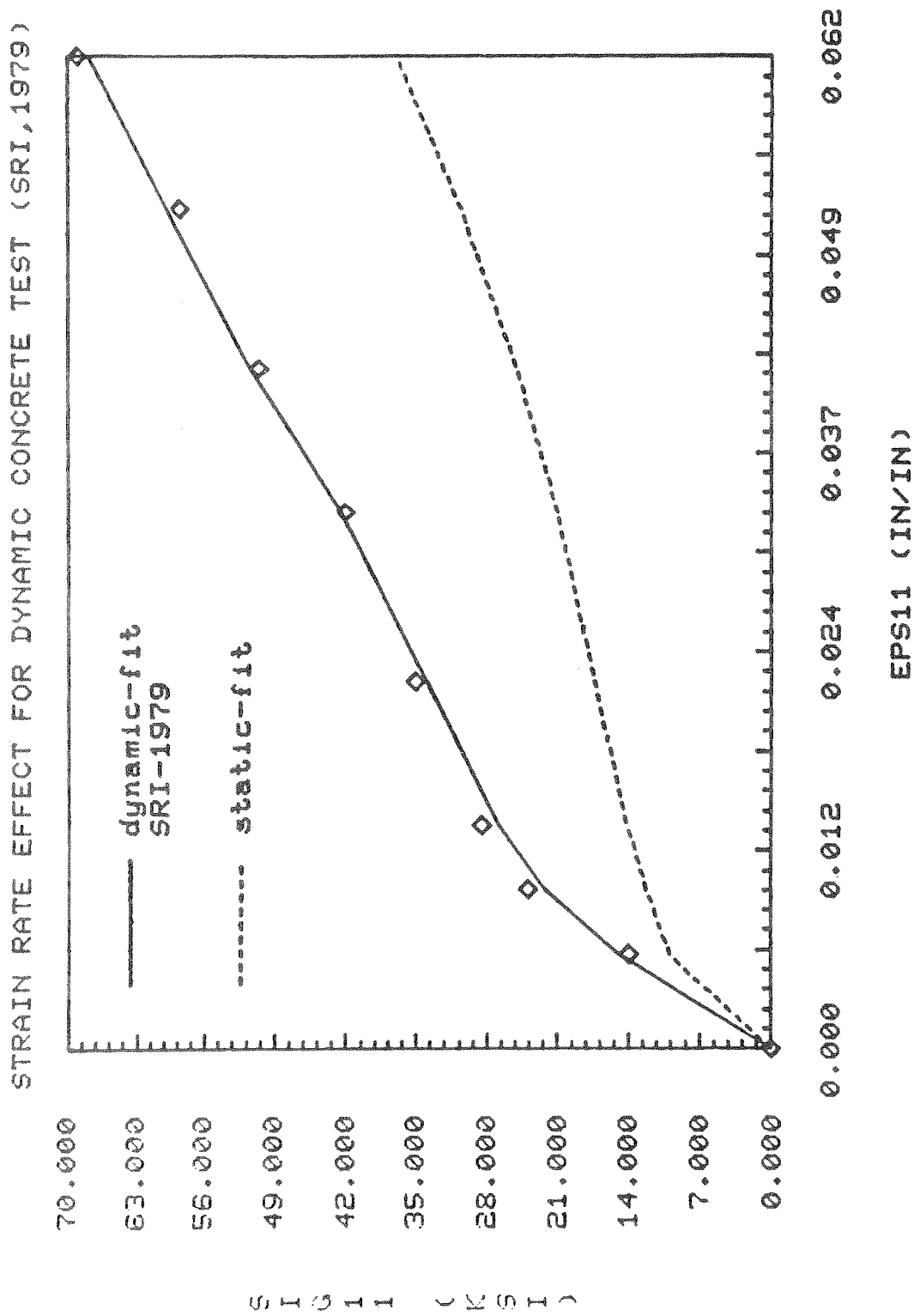


Figure 20. Viscoplastic simulation of the SRI Dynamic Concrete Test (1979). This is a dynamic uniaxial strain history. The diamonds are observed data and the solid-line is a simulated response curve using the viscoplastic cap algorithm. The dash-line is the inviscid limit of the viscoplastic model.

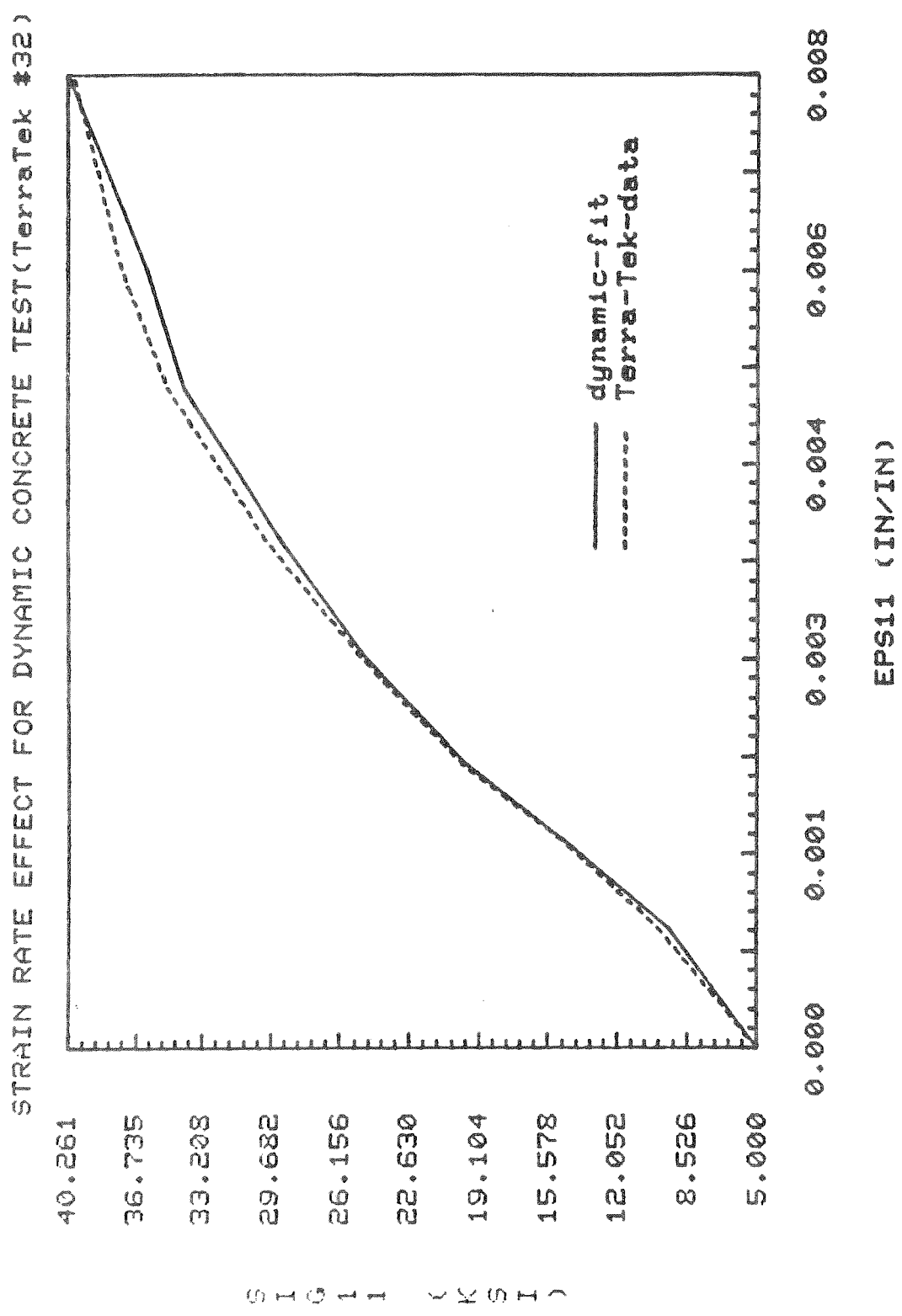


Figure 21. Viscoplastic simulation of the TerraTek Dynamic Concrete Test #32 (1984). This is a dynamic triaxial compression test. The solid-line is observed data and the dash-line is a simulated response curve using the viscoplastic cap algorithm.